ÉCOLE POLYTECHNIQUE
FÉDÉRALE DE LAUSANNE

MATHICSE
Mathematics Institute of Computational Science and Engineering
School of Basic Sciences - Section of Mathematics

MATHICSE Technical Report
Nr. 21.2014
April 2014

Isogeometric numerical dispersion analysis for elastic wave propagation

Luca Dedè, Christoph Jäggli, Alfio Quarteroni

http://mathicse.epfl.ch

Phone: +41 21 69 37648

Address:
EPFL - SB - MATHICSE (Bâtiment MA)
Station 8 - CH-1015 - Lausanne - Switzerland

Fax: +41 21 69 32545

Isogeometric numerical dispersion analysis for elastic wave propagation

Luca Dedè [1,*], Christoph Jäggli [2], and Alfio Quarteroni [1,3]

[1] CMCS – Chair of Modeling and Scientific Computing
MATHICSE – Mathematics Institute of Computational Science and Engineering
EPFL – École Polytechnique Fédérale de Lausanne
Station 8, Lausanne, CH–1015, Switzerland

[2] SMA – Mathematics Section
EPFL – École Polytechnique Fédérale de Lausanne
Station 8, Lausanne, CH–1015, Switzerland

[3] MOX – Modeling and Scientific Computing
Department of Mathematics
Politecnico di Milano
Piazza L. da Vinci 32, Milano, 20133, Italy (on leave)

April 25, 2014

Abstract

In this paper, we carry out a numerical dispersion analysis for the linear elastodynamics equations approximated by means of NURBS–based Isogeometric Analysis in the framework of the Galerkin method; specifically, we consider the analysis of harmonic plane waves in an isotropic and homogeneous elastic medium. We compare and discuss the errors associated to the compressional and shear wave velocities and we provide the anisotropic curves for numerical approximations obtained by considering B–splines and NURBS basis functions of different regularity, namely globally C^0– and C^{p-1}–continuous, being p the polynomial degree. We conclude our analysis by numerically simulating the seismic wave propagation in a sinusoidal shaped valley with discontinuous elastic parameters across an internal interface.

Key words. Elastodynamics; Elastic waves propagation; Isogeometric Analysis; Numerical dispersion analysis.

[*]Corresponding author. E–mail: luca.dede@epfl.ch, Phone: +41 21 6930318, Fax: +41 21 6935510.

1 Introduction

In the last decade, Isogeometric Analysis (IGA) [18, 29] has emerged as a methodology aiming at encapsulating the exact geometrical representation of the computational domain, namely the field of Computational Geometry (see e.g. [24]), into the numerical approximation of Partial Differential Equations (PDEs). This integration is made possible by the use of the same basis functions considered for the geometrical representation also for the approximation of the unknown solution fields of the PDEs, introducing the so–called Isogeometric concept [29]. B–splines and Non Uniform Rational B–splines (NURBS) basis functions [35] have mostly been considered for the IGA methodology being the foundations of Computer Aided Design (CAD) systems, even if other geometrical representations as T–splines [41] have been employed as well for their flexibility; see e.g. [9]. So far, NURBS–based IGA has been mostly used in the framework of the Galerkin method [18, 29], even if collocation techniques are recently receiving growing attention [6, 40]. The advantages of the IGA methodology in terms of the "exact" geometrical representation have been exploited in several applications, as e.g. structural mechanics [12, 29, 32] and fluid dynamics [10, 11, 46] among the most common. Moreover, the use of B–splines and NURBS basis functions in IGA possess several advantages in the numerical approximation of PDEs regardless of the geometrical considerations, as highlighted, e.g., in fluid dynamics [2], structural dynamics [21, 38], high–order PDEs [44], and phase field problems [27, 33]. Such advantages include the possibility of using globally C^{p-1}–continuous basis functions, p being the polynomial degree, and the k–refinement strategy, a procedure for the "enrichment" of the discrete function spaces peculiar of B–splines and NURBS for which the degree and global continuity of the basis functions are increased; see e.g. [19, 26]. In particular, the use of globally C^{p-1}–continuous NURBS basis functions has been shown to be superior to its Finite Elements counterpart of polynomial degree p by means of extensive spectrum and dissipation analyses, both in terms of analytical and numerical results for $1D$, $2D$, and $3D$ structural, vibration, acoustic, and wave propagation problems [18, 19, 20, 21, 30, 38].

Numerical (grid) dispersion analysis for the linear elastodynamics equations, i.e for linear wave propagation in an elastic medium, is often used to assess the accuracy of numerical schemes for applications in civil, geophysics, and earthquake engineering. Such analysis has been extensively carried out for the Finite Elements method [3, 45], Discontinuous Galerkin methods [4, 16, 23, 28, 39], and the Spectral (element) method [22, 34, 42], including non–conforming high–order discretizations [5]. In [20] a numerical dispersion analysis has been performed for NURBS–based IGA for the Helmholtz equation in the $1D$ setting on an infinite line, including linear and p– and k–refined quadratic approximations. This analysis has been extended in [30] to higher degree NURBS basis functions for vibration problems of rods and beams of finite length. In addition, a numerical dispersion analysis for $2D$ vibration problems described by the Helmholtz equation is reported in [30] for the special case of a bilinear approximation; the associated anisotropic (dispersion) curve is also reported for this case only.

In this respect, in this paper we propose a numerical dispersion analysis for the elastodynamics equations, specifically for the linear wave propagation in an isotropic elastic medium, in terms of the spatial approximation by means of NURBS–based IGA in the framework of the Galerkin method. We report for the first time the anisotropic curves and errors associated to the compressional and shear wave velocities in the elastic medium by considering both B–splines and NURBS basis functions and different material properties (characterized by their Poisson ratio). Specifically, in our numerical comparison, we consider B–splines and NURBS basis functions of different polynomial degrees p with particular emphasis on their regularity properties, i.e. their global C^0– or C^{p-1}–

continuity in the computational domain (this corresponds to either p– or k–refinement, see [19, 26]). Our dispersion analysis is based on the procedure proposed in [42] for the coherent comparison of numerical schemes in bounded computational domains for different wave directions without the need to strongly enforce periodic boundary conditions. Specifically, we adapt the approach of [42], originally developed for Spectral (element) methods, to NURBS–based IGA in the framework of the Galerkin method with the aim of consistently comparing the results obtained with basis functions of different polynomial degrees p and global C^0– and C^{p-1}–continuity.

We conclude our analysis by numerically simulating a seismic event, i.e. an elastic wave propagation problem, in a $2D$ portion of the earth mantle embedding a sinusoidal type valley. The latter is delimited by an internal interface, which separates two regions with discontinuous material parameters (different media); such configuration is suitably represented by means of C^0/C^1–continuous B–splines basis functions. For the numerical simulation of this seismic event, we use NURBS–based IGA for the spatial approximation and the generalized–α method ([17]) for the time discretization with a fully implicit scheme. Through this example we numerically highlight the suitability of NURBS–based IGA to solve elastodynamics problems with discontinuous material properties across internal interfaces.

The paper is organized as follows. In Sec. 2 we briefly recall the linear elastodynamics model used in seismic applications. Sec. 3 introduces to B–splines and NURBS basis functions, geometrical representations, and the Isogeometric concept. In Sec.4 we discuss the spatial approximation of the elastodynamics equations by means of NURBS–based IGA in the framework of the Galerkin method, as well as the time discretization. In Sec. 5 we carry out the numerical dispersion analysis for the problem at hand and specific for NURBS basis functions of different regularity; next, we report and discuss the associated numerical results. In Sec. 6 we numerically simulate a seismic event by solving the elastic wave propagation problem in a sinusoidal valley. Conclusions follow.

2 Mathematical Model

In this section we introduce the elastodynamics model, namely the linear elastic equation for a compressible medium in the standard displacement formulation, similarly to [5].

Let us assume that an elastic medium is represented by an open spatial domain $\Omega \subset \mathbb{R}^d$ ($|\Omega| < +\infty$) with $d = 2, 3$. We denote the boundary of Ω as $\partial\Omega$ and we partition it into the subsets Γ_D, Γ_N, and Γ_{NR} such that $\mathring{\Gamma}_D \cap \mathring{\Gamma}_N = \mathring{\Gamma}_D \cap \mathring{\Gamma}_{NR} = \mathring{\Gamma}_N \cap \mathring{\Gamma}_{NR} = \emptyset$ and $\partial\Omega = \overline{\Gamma_D \cup \Gamma_N \cup \Gamma_{NR}}$; we also indicate with $\widehat{\boldsymbol{n}}$ the outward directed, unit vector normal to $\partial\Omega$. We are interested in determining the displacement of the medium, say $\boldsymbol{u} = (u_1, \ldots, u_d)^{\mathrm{T}} = \boldsymbol{u}(\mathbf{x}, t)$, in terms of the spatial $\mathbf{x} \in \Omega$ and temporal $t \in (0, T)$ independent variables under the action of external forces, where T delimits the time interval such that $0 < T < +\infty$. The displacement based equilibrium equations for a linear elastic medium, endowed with suitable boundary and initial conditions, read:

$$\text{find } \boldsymbol{u} : \Omega \times (0,T) \to \mathbb{R}^d \quad : \quad \begin{cases} \rho \dfrac{\partial^2 \boldsymbol{u}}{\partial t^2}(t) - \nabla \cdot \underline{\boldsymbol{\sigma}}(\boldsymbol{u}(t)) = \boldsymbol{f}(t) & \text{in } \Omega \times (0,T), \\ \boldsymbol{u}(t) = \boldsymbol{g} & \text{on } \Gamma_D \times (0,T), \\ \underline{\boldsymbol{\sigma}}(\boldsymbol{u}(t))\widehat{\boldsymbol{n}} = \boldsymbol{h}(t) & \text{on } \Gamma_N \times (0,T), \\ \text{non–reflecting b.c.s} & \text{on } \Gamma_{NR} \times (0,T), \\ \dfrac{\partial \boldsymbol{u}}{\partial t}(0) = \dot{\boldsymbol{u}}_0 & \text{in } \Omega, \\ \boldsymbol{u}(0) = \boldsymbol{u}_0 & \text{in } \Omega, \end{cases} \tag{2.1}$$

where $\underline{\boldsymbol{\sigma}}(\boldsymbol{u})$ is the *stress tensor* (defined later), $\boldsymbol{f} = \boldsymbol{f}(\mathbf{x}, t)$ is the vector of external forces, ρ the medium density, $\boldsymbol{g} = \boldsymbol{g}(\mathbf{x})$ and $\boldsymbol{h} = \boldsymbol{h}(\mathbf{x}, t)$ are sufficiently smooth boundary data, and the initial data $\dot{\boldsymbol{u}}_0 = \dot{\boldsymbol{u}}_0(\mathbf{x})$, $\boldsymbol{u}_0 = \boldsymbol{u}_0(\mathbf{x})$ are given and sufficiently smooth functions in Ω; non–reflecting boundary conditions will be specified later on Γ_{NR}. We remark that the explicit dependency of the variables on the spatial coordinates in Eq. (2.1) has been omitted. By defining the strain tensor as $\underline{\boldsymbol{\epsilon}}(\boldsymbol{u}) = \frac{1}{2}(\nabla \boldsymbol{u} + \nabla \boldsymbol{u}^{\mathrm{T}})$, the stress tensor $\underline{\boldsymbol{\sigma}}(\boldsymbol{u})$ satisfies the constitutive relation $\underline{\boldsymbol{\sigma}}(\boldsymbol{u}) = \lambda\,(\nabla \cdot \boldsymbol{u})\mathrm{I} + 2\mu\,\underline{\boldsymbol{\epsilon}}(\boldsymbol{u})$, where λ and μ are the Lamé elasticity coefficients of the medium; the latter are expressed in terms of the Young modulus E and Poisson's ratio ν as $\lambda = \dfrac{\nu\, E}{(1+\nu)\,(1-2\nu)}$ and $\mu = \dfrac{E}{2(1+\nu)}$, respectively. Also, we introduce the *shear* c_s and the *compressional* c_p *wave velocities* defined as:

$$c_s := \sqrt{\frac{\mu}{\rho}} \qquad \text{and} \qquad c_p := \sqrt{\frac{\lambda + 2\mu}{\rho}}, \tag{2.2}$$

respectively. In order to include a damping factor into the linear elastic equation, we introduce an internal forcing term $\boldsymbol{f}^{visc}(\boldsymbol{u}) := -2\rho\,\zeta\,\dfrac{\partial \boldsymbol{u}}{\partial t} - \rho\,\zeta^2\,\boldsymbol{u}$, where ζ is a suitable *decay factor*, dimensionally consistent with the inverse of time. Therefore, the equilibrium equation (2.1) with damping term reads:

$$\rho\,\frac{\partial^2 \boldsymbol{u}}{\partial t^2}(t) - \nabla \cdot \underline{\boldsymbol{\sigma}}(\boldsymbol{u})(t) - \boldsymbol{f}^{visc}(\boldsymbol{u}(t)) = \boldsymbol{f}(t) \qquad \text{in } \Omega \times (0,T). \tag{2.3}$$

On the subset Γ_{NR} of the boundary we introduce a fictitious traction, being a linear combination of time and space derivatives, in order to set the non–reflecting boundary conditions. Similarly to [5], by introducing the tangential unit vector $\widehat{\boldsymbol{\tau}}$ such that $\widehat{\boldsymbol{\tau}} \cdot \widehat{\boldsymbol{n}} = 0$ on Γ_{NR}, the non–reflecting boundary conditions of Eq.(2.1) read, for example in the two–dimensional case ($d = 2$) :

$$\begin{cases} \dfrac{\partial}{\partial n}(\boldsymbol{u} \cdot \widehat{\boldsymbol{n}}) = -\dfrac{1}{c_p}\dfrac{\partial}{\partial t}(\boldsymbol{u} \cdot \widehat{\boldsymbol{n}}) + \dfrac{c_s - c_p}{c_p}\dfrac{\partial}{\partial \tau}(\boldsymbol{u} \cdot \widehat{\boldsymbol{\tau}}), \\ \dfrac{\partial}{\partial n}(\boldsymbol{u} \cdot \widehat{\boldsymbol{\tau}}) = -\dfrac{1}{c_s}\dfrac{\partial}{\partial t}(\boldsymbol{u} \cdot \widehat{\boldsymbol{\tau}}) + \dfrac{c_s - c_p}{c_p}\dfrac{\partial}{\partial \tau}(\boldsymbol{u} \cdot \widehat{\boldsymbol{n}}), \end{cases} \qquad \text{on } \Gamma_{NR} \times (0,T), \tag{2.4}$$

where the coordinates $\{n, \tau\}$, which are defined by the vectors $\widehat{\boldsymbol{n}}$ and $\widehat{\boldsymbol{\tau}}$, have been considered. We refer the reader to [15, 43] for the general form of the non–reflecting boundary conditions in the three–dimensional case ($d = 3$).

3 B–splines and NURBS: the Isogeometric Concept

In this section we briefly recall the B–splines and NURBS basis functions, their properties, their use for the geometrical representation of computational domains, and the so called Isogeometric concept. For a more detailed review of the topic, we refer the interested reader to [35].

3.1 B–splines basis functions

A univariate B–Spline basis function is a piecewise polynomial of a given degree $p \in \mathbb{N}$; specifically, a B–spline basis is represented by $n \in \mathbb{N}$ basis functions, determined from a *knot vector*, that is an ordered set $\Xi = \{\xi_1, \ldots, \xi_{n+p+1}\}$ of real values. Specifically, we consider open knot vectors, for

which the first and last knots of Ξ are repeated $p+1$ times. The interval $\widehat{\Omega} = (\xi_1, \xi_{n+p+1}) \subset \mathbb{R}$ determines a patch or a *parameter domain*, while (ξ_i, ξ_{i+1}), for some $i = p+1, \ldots, n$, identifies a knot span. If the size of a knot span is greater than zero, it is called *mesh element* in the parameter domain $\widehat{\Omega}$ and denoted as $\widehat{K}_j$ for some $j = 1, \ldots, n_{el}$, where n_{el} is the number of mesh elements in the parameter domain; the set of mesh elements in the parameter domain is simply called *mesh* of the parameter domain, say $\widehat{\mathcal{K}}_h := \left\{ \widehat{K}_j \,:\, j = 1, \ldots, n_{el} \right\}$. A B–spline basis $\{N_{i,p}(\xi)\}_{i=1}^{n}$ is determined by the basis functions $N_{i,p}(\xi)$ for some $i = 1, \ldots, n$ by using the Cox–de Boor recursive formula; starting from $q = 0$ we define:

$$N_{i,0}(\xi) = \begin{cases} 1 & \text{if } \ \xi_i \le \xi < \xi_{i+1}, \\ 0 & \text{otherwise,} \end{cases} \qquad i = 1, \ldots, n+p \tag{3.1}$$

and, for $q = 1, \ldots, p$:

$$N_{i,q}(\xi) = \frac{\xi - \xi_i}{\xi_{i+q} - \xi_i} N_{i,q-1}(\xi) + \frac{\xi_{i+q+1} - \xi}{\xi_{i+q+1} - \xi_{i+1}} N_{i+1,q-1}(\xi), \qquad i = 1, \ldots, n+p-q, \tag{3.2}$$

under the assumption that $\dfrac{0}{0} = 0$. The global regularity of B–splines basis functions in the parameter domain depends on the knot vector, namely on the multiplicity of the knots. Indeed, the basis functions are C^∞–continuous inside each element of non–zero size; however, if a knot value ξ_i is repeated $1 \le m_i \le p+1$ times, the basis functions possess only $p - m_i$ continuous derivatives across ξ_i. Therefore, a B–spline basis function is globally C^α–continuous in the parameter domain $\widehat{\Omega}$ if the internal knots of Ξ are repeated at most m times, where $\alpha = p - m$ and $m = \max\limits_{i=p+2,\ldots,n} m_i$. We obtain the following algebraic relation between the number of mesh elements $n_{el} > 1$ and the number of basis functions, say n_α, depending on their C^α–continuity across each internal knot:

$$n_\alpha = (p - \alpha)\, n_{el} + \alpha + 1 \qquad \text{for } \alpha = 0, \ldots, p-1. \tag{3.3}$$

As we can observe, the number of basis functions for a fixed number of mesh elements n_{el} increases when the regularity of the basis functions α decreases.

As examples of univariate B–splines basis functions of different regularities, we consider in Fig. 1 the polynomial oders $p = 2$ or 3 and the open knot vectors with internal knots $1/4, 1/2$, and $3/4$ with different multiplicities, being 0 the first knot and 1 the last. Finally, among the properties of B–splines basis functions, we recall that they are pointwise non–negative ($N_{i,p}(\xi) \ge 0$ for all $\xi \in \widehat{\Omega}$), represent a partition of the unity ($\sum\limits_{i=1}^{n} N_{i,p}(\xi) = 1$ for all $\xi \in \widehat{\Omega}$), and possess compact support in $p+1$ knot spans; therefore, there are $p+1$ basis functions with support in each knot span (ξ_i, ξ_{i+1}), for all $i = 1, \ldots, n+p$.

Multivariate B–splines basis functions are built by means of the tensor product of univariate basis functions. For example, let $\Xi = \{\xi_1, \ldots, \xi_{n+p+1}\}$ and $\mathcal{H} = \{\eta_1, \ldots, \eta_{m+q+1}\}$ be two knot vectors, then, the bivariate B–splines basis functions are defined in the parameter domain $\widehat{\Omega} = (\xi_1, \xi_{n+p+1}) \times (\eta_1, \eta_{m+q+1})$ for $\boldsymbol{\xi} = (\xi, \eta)$ such that $Q_{i,p,q}(\boldsymbol{\xi}) = Q_{i,p,q}(\xi, \eta) = N_{j,p}(\xi)\, M_{k,q}(\eta)$ for $i = j + (k-1)n = 1, \ldots, N_{bf}$, with $j = 1, \ldots, n$ and $k = 1, \ldots, m$; $N_{j,p}$ and $M_{k,q}$ are the univariate basis functions built from the knot vectors Ξ and $\mathcal{H}$, respectively and $N_{bf} = n\, m$ indicates the total number of basis functions. The extension to the general multivariate case is straightforward in virtue of the tensor product rule. In this work we consider basis functions for which the same

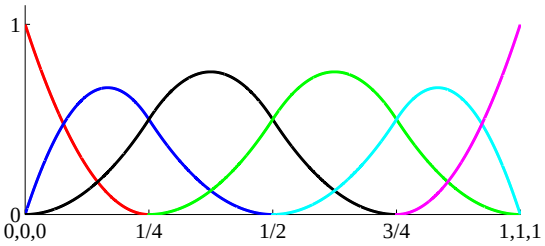

(a) $\Xi = \{0, 0, 0, 1/4, 1/2, 3/4, 1, 1, 1\}$ and $p = 2$; the $n = 6$ basis functions are globally C^1–continuous.

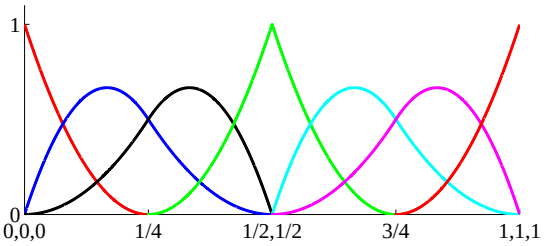

(b) $\Xi = \{0, 0, 0, 1/4, 1/2, 1/2, 3/4, 1, 1, 1\}$ and $p = 2$; the $n = 7$ basis functions are C^1–continuous across the knots $1/4$ and $3/4$, but only C^0–continuous across the knot $1/2$ of multiplicity 2.

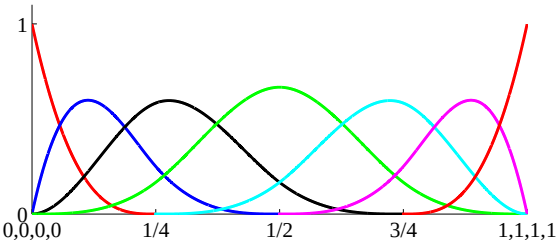

(c) $\Xi = \{0, 0, 0, 0, 1/4, 1/2, 3/4, 1, 1, 1, 1\}$ and $p = 3$; the $n = 7$ basis functions are globally C^2–continuous.

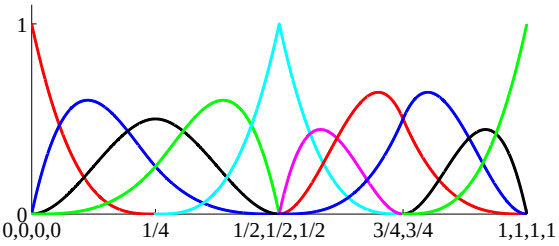

(d) $\Xi = \{0, 0, 0, 0, 1/4, 1/2, 1/2, 1/2, 3/4, 3/4, 1, 1, 1, 1\}$ and $p = 3$; the $n = 10$ basis functions are C^2–continuous across the knot $1/4$, C^1–continuous across the knot $3/4$ of multiplicity 2, and only C^0–continuous across the knot $1/2$ of multiplicity 3.

Figure 1: Univariate B–splines basis functions obtained from open knot vectors Ξ and polynomial degrees $p = 2$ and $p = 3$ with different regularities.

polynomial degree is used along both the parametric directions, e.g. for which $p = q$ in the bivariate case; therefore, multivariate basis functions will be generically indicated by using the same notation of univariate basis functions, i.e. $N_{i,p}$ for some $i = 1, \dots, N_{bf}$.

We observe that the tensor product structure extends the positivity, the partition of the unity, and the regularity properties of the univariate basis to the multivariate case. Multidimensional mesh elements in the parameter domain are constructed by means of the tensor product of one dimensional mesh elements, similarly to the univariate case; we indicate the set of such mesh elements as $\widehat{\mathcal{K}}_h := \left\{ \widehat{K}_j \, : \, j = 1, \dots, N_{el} \right\}$, where N_{el} is its total number.

3.2 NURBS basis functions

NURBS, Non Uniform Rational B–splines ([35]), are built from B–splines by introducing a set of weights for each basis function. By considering directly the multivariate case for which the same polynomial degree p is considered along all the parametric directions, we introduce the weights $\{w_i\}_{i=1}^{N_{bf}} \subset \mathbb{R}$ and we define the weighting function $W(\boldsymbol{\xi}) = \sum_{i=1}^{N_{bf}} N_{i,p}(\boldsymbol{\xi})\, w_i$, where $\{N_{i,p}(\boldsymbol{\xi})\}_{i=1}^{n}$ are the B–splines basis functions. In our analysis, we bound ourself to the standard case of weights

real and strictly positive. We define a set of NURBS basis functions $\{R_{i,p}(\boldsymbol{\xi})\}_{i=1}^{n}$ as:

$$R_{i,p}(\boldsymbol{\xi}) := \frac{N_{i,p}(\boldsymbol{\xi})\, w_i}{W(\boldsymbol{\xi})} \qquad i = 1, \ldots, N_{bf}, \tag{3.4}$$

that is the ratio of two piecewise polynomials, both of degree p; therefore, we refer to p as the degree of the NURBS basis functions. It is straightforward to see that NURBS basis functions still satisfy the same properties of B–splines basis functions. We notice that B–splines are a particular case of NURBS by construction, obtained by setting all the weights to the same value; henceforth we will use the notation $R_{i,p}$, for some $i = 1, \ldots, N_{bf}$, to indicate indifferently a B–splines or NURBS basis function.

We remark that the NURBS and B–splines bases can be enriched by using the so called h– or p–refinement procedures obtained by means of the knot insertion and order elevation techniques, respectively. In addition, the k–refinement procedure, which is peculiar of the B–splines and NURBS and consists in the sequential application of the order elevation and knot insertion techniques on the initial knot vector Ξ, may be used to enrich the basis by introducing a limited number of basis functions. For more information, we refer the reader to [18, 29, 35].

3.3 Geometrical representations by B–splines and NURBS

Given a set of univariate B–splines or NURBS basis functions $\{R_{i,p}\}_{i=1}^{N_{bf}}$ and a set of *control points* $\{\boldsymbol{P}_i\}_{i=1}^{N_{bf}} \subset \mathbb{R}^d$ in the physical domain $\mathbb{R}^d$ for $d = 1, 2, 3$, a NURBS geometry is a parametrization $\mathbf{x} : \widehat{\Omega} \to \mathbb{R}^d$ defined as:

$$\mathbf{x}(\boldsymbol{\xi}) = \sum_{i=1}^{N_{bf}} R_{i,p}(\boldsymbol{\xi})\, \boldsymbol{P}_i. \tag{3.5}$$

In this work, we consider the standard case for which the dimension of the physical domain Ω, represented by the geometrical entity $\mathbf{x}$, coincides with that of the parameter domain $\widehat{\Omega} \subset \mathbb{R}^\kappa$, i.e. for which $\kappa \equiv d$. Moreover, we consider the case of bivariate NURBS basis functions, for which $\kappa = 2$, and computational domains Ω in the two–dimensional physical space $\mathbb{R}^2$, i.e. for which $d = \kappa = 2$.

We remark that the mesh $\widehat{\mathcal{K}}_h$ defined in the parameter domain for the construction of the B–splines and NURBS basis functions yields the mesh $\mathcal{K}_h$ in the physical domain Ω in virtue of the geometrical mapping (3.5), i.e. $\mathcal{K}_h := \{K_j : j = 1, \ldots, N_{el}\}$, where K_j is the geometrical mapping of the element $\widehat{K}_j$ in the parameter domain $\widehat{\Omega}$ for some $j = 1, \ldots, N_{el}$. Finally, we observe that when the h–, p–, or k–refinement procedures are used, the geometrical representation (3.5) is preserved in the sense that the geometrical mapping $\mathbf{x}(\boldsymbol{\xi})$ and its Jacobian remain the same for all the applied refinement procedures.

3.4 The Isogeometric concept

Let us assume that a physical (computational) domain Ω is represented by means of the B–splines or NURBS geometrical mapping (3.5) from a parameter domain $\widehat{\Omega}$ by using the basis functions $R_{i,p}$ for $i = 1, \ldots, N_{bf}$; in addition, let us assume that a function $\widehat{u}_h = \widehat{u}_h(\boldsymbol{\xi})$ is defined in $\widehat{\Omega}$, as e.g. the approximate solution of a scalar PDE. Then, according to the *Isoparametric concept*, any candidate to represent each scalar component of the solution approximating the solution $\boldsymbol{u}$ in Eq. (2.1) at

any t will feature the following expansion with respect to the spatial parametric coordinate:

$$\widehat{u}_h(\xi) = \sum_{i=1}^{N_{bf}} R_{i,p}(\boldsymbol{\xi})\, U_i, \tag{3.6}$$

where $R_{i,p}$, for $i = 1, \ldots, N_{bf}$, are the same NURBS basis functions used in the geometrical representation (3.5) and the coefficients $U_i \in \mathbb{R}$ are the corresponding control variables. We remark that the properties of the function $\widehat{u}_h$ follows from those of the B–splines or NURBS basis functions. By assuming that the geometrical mapping $\mathbf{x}(\boldsymbol{\xi})$ of Eq. (3.5) is invertible, the function $\widehat{u}_h$ can be rewritten in the physical domain Ω as $u_h : \Omega \to \mathbb{R}$ reading:

$$u_h = \hat{u}_h \circ \mathbf{x}^{-1}. \tag{3.7}$$

For simplicity, in virtue of the invertibility of the geometrical mapping $\mathbf{x}(\boldsymbol{\xi})$, here henceforth we will not distinguish between $\widehat{u}_h$ and u_h by writing u_h regardless which domain, parametric $\widehat{\Omega}$ or physical Ω, we are referring to.

Finally, in view of the use of the Isogeometric concept in the framework of the Galerkin method, it is convenient to introduce the B–splines and NURBS function spaces. By using the B–splines or NURBS basis functions introduced in Secs. 3.1 and 3.2, we can define the finite dimensional B–splines or NURBS function space as:

$$\mathcal{N}_h := \operatorname{span}\left\{R_{i,p},\ i = 1, \ldots, N_{bf}\right\}, \tag{3.8}$$

with N_{bf} its dimension.

4 Numerical Approximation of PDEs: Isogeometric Analysis

We discuss the numerical approximation of the elastodynamics equations described in Sec. 2. For the spatial approximation we consider NURBS–based IGA in the framework of the Galerkin method [18, 29], while the generalized–α method for the time discretization [17].

4.1 Spatial approximation: NURBS–based IGA

Let us introduce the space of square integrable functions in Ω, i.e. $L^2(\Omega)$, and the Hilbert space $H^1(\Omega) = \{v : \Omega \to \mathbb{R}^d$ such that $D^{\boldsymbol{\alpha}} v \in L^2(\Omega)$ and $|\boldsymbol{\alpha}| \leq 1\}$, where $\boldsymbol{\alpha} = \{\alpha_1, \ldots, \alpha_d\} \in \mathbb{N}^d$ is a multi–index, $|\boldsymbol{\alpha}| = \sum_{i=1}^{d} \alpha_i$ and $D^{\boldsymbol{\alpha}}$ the multi–index distributional derivative operator; see e.g. [1]. By referring to Eq. (2.1), we set the trial function space $\mathcal{S}$ (actually, an affine manifold):

$$\mathcal{S} := \{\boldsymbol{v} : \Omega \to \mathbb{R} \text{ such that } \boldsymbol{v} \in \left[H^1(\Omega)\right]^d \text{ and } v_i|_{\Gamma_D} = g_i,\ \forall\, i = 1, \ldots, d\}, \tag{4.1}$$

where $\Gamma_D \subset \partial\Omega$ and v_i denotes the i–th components of the vector $\boldsymbol{v}$, and the test function space:

$$\mathcal{V} := \{\boldsymbol{w} : \Omega \to \mathbb{R}^d \text{ such that } \boldsymbol{w} \in \left[H^1(\Omega)\right]^d \text{ and } \boldsymbol{w}|_{\Gamma_D} = \mathbf{0}\}. \tag{4.2}$$

Let us define the bilinear forms $\mathcal{A}$, a, c, $m : \mathcal{V} \times \mathcal{S} \to \mathbb{R}$ from Eqs. (2.1) and (2.3) as:

$$\begin{aligned} &\mathcal{A}(\boldsymbol{w},\boldsymbol{u}) = a(\boldsymbol{w},\boldsymbol{u}) + c(\boldsymbol{w},\boldsymbol{u}) + m(\boldsymbol{w},\boldsymbol{u}), && a(\boldsymbol{w},\boldsymbol{u}) = \int_\Omega \underline{\boldsymbol{\sigma}}(\boldsymbol{u}) : \underline{\boldsymbol{\epsilon}}(\boldsymbol{w})\, d\Omega + \int_\Omega \rho\zeta^2\, \boldsymbol{u}\cdot\boldsymbol{w}\, d\Omega, \\ &c(\boldsymbol{w},\boldsymbol{u}) = \int_\Omega 2\rho\zeta\, \frac{\partial \boldsymbol{u}}{\partial t}\cdot\boldsymbol{w}\, d\Omega, && m(\boldsymbol{w},\boldsymbol{u}) = \int_\Omega \rho\, \frac{\partial^2 \boldsymbol{u}}{\partial t^2}\cdot\boldsymbol{w}\, d\Omega \end{aligned} \tag{4.3}$$

and the linear functional $F : \mathcal{V} \to \mathcal{R}$:

$$F(\boldsymbol{w};t) = \int_\Omega \boldsymbol{f}(t)\cdot\boldsymbol{w}\, d\Omega + \oint_{\Gamma_N} \boldsymbol{h}(t)\cdot\boldsymbol{w}\, d\Omega. \tag{4.4}$$

Then, the weak form of the linear elastodynamics equation (2.1) with viscous terms (2.3), in the case $\Gamma_{NR} = \emptyset$, reads:

$$\text{find } \boldsymbol{u}(t) \in \mathcal{S} \quad : \quad \mathcal{A}(\boldsymbol{w},\boldsymbol{u}(t)) = F(\boldsymbol{w};t) \qquad \forall \boldsymbol{w} \in \mathcal{V},\ \forall t \in (0,T), \tag{4.5}$$

for $\boldsymbol{u}(0) = \boldsymbol{u}_0$ and $\dot{\boldsymbol{u}}(0) = \dot{\boldsymbol{u}}_0$. We remark that the bilinear form $\mathcal{A}(\cdot,\cdot)$ and the linear functional $F(\cdot;t)$ can be suitably modified to take into account for the non–reflecting boundary conditions (2.4) on $\Gamma_{NR} \subset \partial\Omega$ in the case in which $\Gamma_{NR} \neq \emptyset$.

Let us introduce two suitable finite dimensional subspaces $\mathcal{S}_h \subset \mathcal{S}$ and $\mathcal{V}_h \subset \mathcal{V}$; specifically, by using the Isogeometric concept of Sec. 3.4 and the B–splines or NURBS function space $\mathcal{N}_h$ of Eq. (3.8), we set $\mathcal{S}_h = \mathcal{S} \cap [\mathcal{N}_h]^d$ and $\mathcal{V}_h = \mathcal{V} \cap [\mathcal{N}_h]^d$ ([1]). Then the approximation of the problem (4.5) by means of NURBS–based IGA in the framework of the Galerkin method reads:

$$\text{find } \boldsymbol{u}_h(t) \in \mathcal{S}_h \quad : \quad \mathcal{A}(\boldsymbol{w}_h,\boldsymbol{u}_h(t)) = F(\boldsymbol{w}_h;t) \qquad \forall \boldsymbol{w}_h \in \mathcal{V}_h,\ \forall t \in (0,T). \tag{4.6}$$

The problem (4.6) is in semi–discrete form with the approximate solution reading $\boldsymbol{u}_h(t) = (u_{1,h}(t),\ldots,u_{d,h}(t))^{\mathrm{T}} : \Omega \to \mathbb{R}^d$, with $u_{A,h} = \sum_{i=1}^{N_{bf}} R_{i,p}\, U_{A,i}(t)$, being $\{U_{A,i}\}_{i=1}^{N_{bf}}$ the time dependent control variables for each vectorial component $A = 1,\ldots,d$; the vector of control variables is $\boldsymbol{U}(t) = \left(\boldsymbol{U}_1^{\mathrm{T}}(t),\ldots,\boldsymbol{U}_d^{\mathrm{T}}(t)\right)^{\mathrm{T}} \in \mathbb{R}^{(d\,N_{bf})}$. However, by taking into account the strong imposition of the essential boundary conditions and indicating with N_h the dimension of the function space $\mathcal{S}_h$, for which generally $N_h \leq d\,N_{bf}$, we still refer to the vector of control variables as $\boldsymbol{U}(t) \in \mathbb{R}^{N_h}$ for the sake of simplicity. Also, we indicate with $\boldsymbol{\mathcal{M}}$, $\boldsymbol{\mathcal{C}}$, $\boldsymbol{\mathcal{K}} \in \mathbb{R}^{N_h \times N_h}$ and $\boldsymbol{F}(t) \in \mathbb{R}^{N_h}$ the mass, damping, stiffness matrices, and vector of external forces obtained by the spatial discretization of the forms $m(\cdot,\cdot)$, $c(\cdot,\cdot)$, and $a(\cdot,\cdot)$, and the functional $F(\cdot;t)$, respectively; similarly, $\boldsymbol{U}_0$ and $\dot{\boldsymbol{U}}_0$ represent the L^2–projections of the initial data $\boldsymbol{u}_0$ and $\dot{\boldsymbol{u}}_0$ onto $\mathcal{N}_h$, respectively. Then, the semi–discrete problem reads:

$$\text{find } \boldsymbol{U} : (0,T) \to \mathbb{R}^{N_h} \quad : \quad \begin{cases} \boldsymbol{\mathcal{M}}\,\ddot{\boldsymbol{U}}(t) + \boldsymbol{\mathcal{C}}\,\dot{\boldsymbol{U}}(t) + \boldsymbol{\mathcal{K}}\,\boldsymbol{U}(t) = \boldsymbol{F}(t) \qquad \forall t \in (0,T), \\ \boldsymbol{U}(0) = \boldsymbol{U}_0, \\ \dot{\boldsymbol{U}}(0) = \dot{\boldsymbol{U}}_0, \end{cases} \tag{4.7}$$

where $\dot{\boldsymbol{U}}(t)$ and $\ddot{\boldsymbol{U}}(t)$ are the time derivatives of the displacement vector $\boldsymbol{U}(t)$.

[1] We assume that the Dirichlet data $\boldsymbol{g}$ belongs to the restriction of the NURBS space $[\mathcal{N}_h]^d$ onto Γ_D; see Eq. (2.1).

We remark that the matrices $\boldsymbol{\mathcal{M}}$, $\boldsymbol{\mathcal{C}}$, and $\boldsymbol{\mathcal{K}}$ and the vector $\boldsymbol{F}(t)$ are assembled from the corresponding bilinear forms and linear functional by means of suitable quadrature formulas for the evaluation of the integrals. In IGA a standard procedure consists in using the d–dimensional Gauss–Legendre quadrature formula ([36]) induced by the tensor product construction of multivariate basis functions. The quadrature formula is applied at the level of each element of the mesh $\mathcal{K}_h$; more commonly, in virtue of the isogeometric paradigm, the formula is applied in the parametric domain $\widehat{\Omega}$ at the level of the elements $\widehat{K} \in \widehat{\mathcal{K}}_h$ or in a parent domain [18]. For example, the integral of a function $\widehat{\varphi}(\boldsymbol{\xi})$ defined in the parametric domain $\widehat{\Omega} \subset \mathbb{R}^2$, i.e. $\widehat{\varphi} : \widehat{\Omega} \to \mathbb{R}$ is approximated as:

$$\int_{\widehat{\Omega}} \widehat{\varphi}(\boldsymbol{\xi})\, d\widehat{\Omega} \simeq \sum_{\widehat{K} \in \widehat{\mathcal{K}}_h} \left[\sum_{j=1}^{r^2} \widehat{\varphi}\left(\boldsymbol{\xi}_j^r\right)\, \widehat{w}_j^r \right], \tag{4.8}$$

where r is the number of quadrature nodes defining the Gauss–Legendre formula, while $\left\{\boldsymbol{\xi}_j^r\right\}_{j=1}^{r^2}$ and $\left\{\widehat{w}_j^r\right\}_{j=1}^{r^2}$ are the quadrature nodes and weights in the parameter domain, respectively. In the standard approach to NURBS–based IGA, we set $r = p+1$, which ensures the exact assembly of the matrices $\boldsymbol{\mathcal{M}}$, $\boldsymbol{\mathcal{C}}$, and $\boldsymbol{\mathcal{K}}$ when B–splines are considered; conversely, the matrices are approximated when NURBS basis functions are considered, even if the same Gauss–Legendre formula with $r = p+1$ is used by convention. We observe that more efficient quadrature formulas than the element–wise Gauss–Legendre formula may be used in NURBS–based IGA by taking advantage of the properties of NURBS basis functions; see [7, 31].

4.2 Time discretization: the generalized–α method

We consider the time discretization of the problem (4.6) by means of the generalized–α method, a family of time integrations schemes for structural dynamics problems, initially proposed in [17]. The method has been introduced to control numerical dissipation at high frequency modes, while minimizing low–frequency dissipation.

Let us partition the time interval $[0, T]$ into N_t sub–intervals of equal size $\Delta t = \dfrac{T}{N_t}$ for which the discrete time steps are $t_n = n\Delta t$ for $n = 0, \ldots, N_t$. Also, let us indicate with $\boldsymbol{d}_n$, $\boldsymbol{v}_n$, and $\boldsymbol{a}_n$ the approximations of the vectors $\boldsymbol{U}(t_n)$, $\dot{\boldsymbol{U}}(t_n)$, $\ddot{\boldsymbol{U}}(t_n)$ at the discrete time step t_n, respectively. Then, one step of the generalized–α method at t_n reads, for any $n = 0, \ldots, N_t - 1$:

$$\begin{aligned} &\text{find } \boldsymbol{d}_{n+1},\, \boldsymbol{v}_{n+1},\, \boldsymbol{a}_{n+1} \in \mathbb{R}^{N_h} \quad : \\ &\qquad \begin{cases} \boldsymbol{d}_{n+1} = \boldsymbol{d}_n + \Delta t\, \boldsymbol{v}_n + \Delta t^2 \left[\left(\dfrac{1}{2} - \beta \right) \boldsymbol{a}_n + \beta\, \boldsymbol{a}_{n+1} \right], \\ \boldsymbol{v}_{n+1} = \boldsymbol{v}_n + \Delta t \left[(1-\gamma)\, \boldsymbol{a}_n + \gamma\, \boldsymbol{a}_{n+1} \right], \\ \boldsymbol{\mathcal{M}}\, \boldsymbol{a}_{n+1-\alpha_m} + \boldsymbol{\mathcal{C}}\, \boldsymbol{v}_{n+1-\alpha_f} + \boldsymbol{\mathcal{K}}\, \boldsymbol{d}_{n+1-\alpha_f} = \boldsymbol{F}(t_{n+1-\alpha_f}), \end{cases} \end{aligned} \tag{4.9}$$

given $\boldsymbol{d}_n$, $\boldsymbol{v}_n$, and $\boldsymbol{a}_n$; the parameters α_m, α_f, γ, and $\beta \in \mathbb{R}$ characterize the method with the following definitions:

$$\begin{aligned} \boldsymbol{d}_{n+1-\alpha_f} &:= (1-\alpha_f)\, \boldsymbol{d}_{n+1} + \alpha_f\, \boldsymbol{d}_n, & \boldsymbol{v}_{n+1-\alpha_f} &:= (1-\alpha_f)\, \boldsymbol{v}_{n+1} + \alpha_f\, \boldsymbol{v}_n, \\ \boldsymbol{a}_{n+1-\alpha_m} &:= (1-\alpha_m)\, \boldsymbol{a}_{n+1} + \alpha_m\, \boldsymbol{a}_n, & t_{n+1-\alpha_f} &:= (1-\alpha_f)\, t_{n+1} + \alpha_f\, t_n, \end{aligned} \tag{4.10}$$

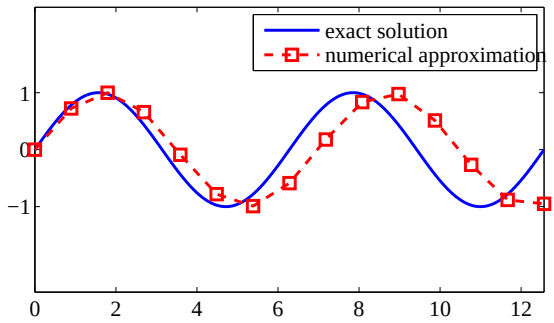

Figure 2: Example of exact and numerical waves; dimensionless quantities on both the axes.

At the time step $t_0 = 0$, we can set $\boldsymbol{d}_0 = \boldsymbol{U}_0$, $\boldsymbol{v}_0 = \dot{\boldsymbol{U}}_0$, and $\boldsymbol{a}_0 = \boldsymbol{\mathcal{M}}^{-1}\left(\boldsymbol{F}(0) - \boldsymbol{\mathcal{C}}\,\dot{\boldsymbol{U}}_0 - \boldsymbol{\mathcal{K}}\,\boldsymbol{U}_0\right)$. We recall that the generalized–α method is a second–order accurate scheme for linear problems, provided that $\gamma = \frac{1}{2} - \alpha_m + \alpha_f$; moreover, it is unconditionally absolutely stable if $\alpha_m \leq \alpha_f \leq \frac{1}{2}$ and $\frac{1}{4} + \frac{1}{2}(\alpha_f - \alpha_m) \leq \beta$. Further, the generalized–α method maximizes high frequency dissipation for $\beta = \frac{1}{4}(1 - \alpha_m + \alpha_f)^2$, while minimizes low frequency dissipation for $\alpha_f = \frac{\alpha_m + 1}{3}$. Following [17] and by introducing the spectral radius of the amplification matrix for $\Delta t \to \infty$, say $\rho_\infty \in [0, 1]$, all the previous properties can be satisfied by choosing the parameters α_m, α_f, γ, and β as:

$$\alpha_m = \frac{2\rho_\infty - 1}{\rho_\infty + 1}, \qquad \alpha_f = \frac{\rho_\infty}{\rho_\infty + 1}, \qquad \beta = \frac{1}{(\rho_\infty + 1)^2}, \qquad \text{and} \qquad \gamma = \frac{3 - \rho_\infty}{2(\rho_\infty + 1)}. \tag{4.11}$$

In this manner, a family of second–order and absolutely stable generalized–α methods controlling the numerical dissipation is defined in terms of the unique parameter ρ_∞.

5 Numerical Dispersion Analysis

In this section, we are interested in quantifying the errors associated with the wave propagation in elastodynamics problems, specifically in evaluating the quality of the numerical wave length and velocities of propagation; see Fig. 2. Due to the mesh structure associated to the spatial approximation method, such errors are dependent on the direction of wave propagation. The analysis of these errors is typically called *numerical* (grid) *dispersion analysis*.

5.1 Harmonic plane waves

Let us consider the isotropic linear elastic equation (2.1) without the source term and in the space–time domain $\Omega \times \mathbb{R}$:

$$\rho \frac{\partial^2 \boldsymbol{u}}{\partial t^2}(t) - \nabla \cdot \underline{\boldsymbol{\sigma}}(\boldsymbol{u}(t)) = \boldsymbol{0} \qquad \text{in } \Omega \times \mathbb{R}. \tag{5.1}$$

In our analysis, we consider the computational domain $\Omega \subset \mathbb{R}^d$ open and bounded, with $d = 2, 3$. In order to study the dispersion of the numerical scheme, we consider particular solutions in the form of harmonic plane waves $\boldsymbol{u}_{PW}(\boldsymbol{k}, \omega) : \Omega \times \mathbb{R} \to \mathbb{R}^d$, reading:

$$\boldsymbol{u}_{PW}(\boldsymbol{k}, \omega) = \boldsymbol{u}_{PW}(\mathbf{x}, t; \boldsymbol{k}, \omega) = \mathrm{e}^{\iota(\boldsymbol{k}\cdot\mathbf{x} - \omega\, t)}\, \boldsymbol{\Psi}, \tag{5.2}$$

where $\omega \in \mathbb{R}$ is the angular frequency, $\boldsymbol{k} = (k_1, \dots, k_d)^{\mathrm{T}} \in \mathbb{R}^d$ is the wave vector, the vector $\boldsymbol{\Psi} = (\Psi_1, \dots, \Psi_d)^{\mathrm{T}} \in \mathbb{R}^d$, which is independent of $\mathbf{x}$ and t, represents the direction and magnitude of the displacement, and ι is the imaginary unit such that $\iota^2 = -1$. For convenience, we rewrite Eq. (5.2) as:

$$\boldsymbol{u}_{PW}(\mathbf{x}, t; \boldsymbol{k}, \omega) = \mathrm{e}^{-\iota\,\omega\,t}\, z_{PW}(\mathbf{x}; \boldsymbol{k})\, \boldsymbol{\Psi} \qquad \text{with } z_{PW}(\mathbf{x}; \boldsymbol{k}) := \mathrm{e}^{\iota\,\boldsymbol{k}\cdot\mathbf{x}}. \tag{5.3}$$

By substituting Eq. (5.2) into Eq. (5.1) and by simplifying for the term $\mathrm{e}^{\iota(\boldsymbol{k}\cdot\mathbf{x}-\omega\,t)}$, we obtain that the plane wave $\boldsymbol{u}_{PW}(t)$ satisfies Eq. (5.1) for some $\boldsymbol{\Psi} \in \mathbb{R}^d$, provided that:

$$-\left(\frac{\omega^2}{\kappa^2} - c_s^2\right)\boldsymbol{\Psi} + (c_p^2 - c_s^2)\left(\boldsymbol{\Psi}\cdot\widehat{\boldsymbol{k}}\right)\widehat{\boldsymbol{k}} = \mathbf{0}, \tag{5.4}$$

where $\kappa := |\boldsymbol{k}|$, $\widehat{\boldsymbol{k}} = \dfrac{\boldsymbol{k}}{\kappa}$ and c_p and c_s are the compressional and shear wave velocities defined in Eq. (2.2), respectively. Eq. (5.4) admits two solutions; the first, say $(\omega_p, \boldsymbol{\Psi}_p)$, such that:

$$\omega_p = \kappa\, c_p \qquad \text{and} \qquad \boldsymbol{\Psi}_p = \alpha_p\, \widehat{\boldsymbol{k}} \qquad \forall \alpha_p \in \mathbb{R}, \tag{5.5}$$

the second, say $(\omega_s, \boldsymbol{\Psi}_s)$, such that:

$$\omega_s = \kappa\, c_s \qquad \text{and} \qquad \boldsymbol{\Psi}_s = \alpha_s\, \widehat{\boldsymbol{n}}_{\boldsymbol{k}} \qquad \forall \alpha_s \in \mathbb{R}, \tag{5.6}$$

where the unit vector $\widehat{\boldsymbol{n}}_{\boldsymbol{k}} \in \mathbb{R}^d$ is normal to $\widehat{\boldsymbol{k}}$, i.e $\widehat{\boldsymbol{n}}_{\boldsymbol{k}} \cdot \widehat{\boldsymbol{k}} = 0$. The first wave, called *compressional wave* or *P–wave*, travels with velocity c_p and induces a displacement in the direction of the wave vector $\widehat{\boldsymbol{k}}$, while the second wave, called *shear wave* or *S–wave*, travels with velocity c_s and induces a displacement orthogonal to $\widehat{\boldsymbol{k}}$, namely along $\widehat{\boldsymbol{n}}_{\boldsymbol{k}}$.

5.2 Formulation of the discrete eigenvalue problem

For the definition of the discrete eigenvalue problem, we consider the approach introduced in [42] for the comparison of different Spectral (element) methods ([13, 14]). The proposed approach is based on the spatial discretization of the elastodynamics equations (5.1) for a general undetermined solution $\boldsymbol{u}(t)$ and the approximation of the harmonic wave particular solution $\boldsymbol{u}_{PW}(\boldsymbol{k}, \omega)$ of Eq. (5.2) by using the same numerical scheme. Then, the discrete wave solution is combined with the discrete elastodynamics wave equation into a discrete eigenvalue problem yielding the discrete angular frequencies corresponding to compressional and shear wave velocities. According to [42], this approach allows the computation of the wave velocities in bounded computational domains Ω without the need of using periodic boundary conditions ([22, 23, 34]), a constraint that would be difficult to fulfill when comparing different numerical schemes for different wave directions $\boldsymbol{k}$.

Let us consider the isotropic elastic wave equation (5.1) endowed with homogeneous Neumann conditions on $\partial\Omega$, i.e. for which $\underline{\boldsymbol{\sigma}}(\boldsymbol{u})\widehat{\boldsymbol{n}} = \mathbf{0}$; then, by setting $\mathcal{S} = \mathcal{V} = \left[H^1(\Omega)\right]^d$, we can rewrite the problem in the weak formulation (4.5). Similarly, the problem approximated with NURBS–based IGA in the framework of the Galerkin method reads as in Eq. (4.6), where the function spaces $\mathcal{S}_h = \mathcal{V}_h$ have dimension $N_h = d\,N_{bf}$; similarly to Eq. (4.7), the matrix–vector form of the discrete problem, which is continuous in time, reads:

$$\text{find } \boldsymbol{U} : \mathbb{R} \to \mathbb{R}^{N_h} \quad : \quad \boldsymbol{\mathcal{M}}\,\ddot{\boldsymbol{U}}(t) + \boldsymbol{\mathcal{K}}\,\boldsymbol{U}(t) = \mathbf{0} \qquad \forall t \in \mathbb{R}, \tag{5.7}$$

Following the approach of [42], we proceed in determining the discrete harmonic plane wave, obtained by L^2–projection of the harmonic plane wave $\boldsymbol{u}_{PW}(\boldsymbol{k},\omega)$ (5.2) onto the NURBS space $\mathcal{N}_h$ (3.8). From Eq. (5.3), we obtain $\widetilde{z}_{PW,h}(\boldsymbol{k}) : \Omega \to \mathbb{R}$, reading $\widetilde{z}_{PW,h}(\boldsymbol{k}) = \sum_{i=1}^{N_{bf}} R_{i,p}\, \widetilde{Z}_{PW,i}(\boldsymbol{k})$, by solving the following L^2–projection problem for some given wave vector $\boldsymbol{k}$:

$$\text{find } \widetilde{z}_{PW,h}(\boldsymbol{k}) \in \mathcal{N}_h \quad : \quad \int_\Omega w_h\, \widetilde{z}_{PW,h}(\boldsymbol{k})\, d\Omega = \int_\Omega w_h\, z_{PW}(\boldsymbol{k})\, d\Omega \qquad \forall w_h \in \mathcal{N}_h, \tag{5.8}$$

with the control variables $\widetilde{\boldsymbol{Z}}_{PW}(\boldsymbol{k}) \in \mathbb{C}^{N_{bf}}$ ([2]). Then, from Eq. (5.8), the discrete harmonic wave, say $\widetilde{\boldsymbol{u}}_{PW,h}(\boldsymbol{k},\omega) : \Omega \times \mathbb{R} \to \mathbb{C}^d$, for $\boldsymbol{k}$ and ω given, reads:

$$\widetilde{\boldsymbol{u}}_{PW,h}(t;\boldsymbol{k},\omega) = \mathrm{e}^{-\imath\,\omega\,t}\, \widetilde{z}_{PW,h}(\boldsymbol{k})\, \boldsymbol{\Psi}. \tag{5.9}$$

We remark that the notation $\widetilde{\boldsymbol{u}}_{PW,h}(t;\boldsymbol{k},\omega)$ is used to indicate that the discrete harmonic plane wave is not obtained by solving the Galerkin problem under the assumption (5.2), which would yield the approximated harmonic plane $\boldsymbol{u}_{PW,h}(t;\boldsymbol{k},\omega)$, but rather its approximation in the NURBS space $\mathcal{N}_h$ by means of L^2–projection. For the sake of simplicity, we rewrite $\widetilde{\boldsymbol{u}}_{PW,h}(t;\boldsymbol{k},\omega)$ in matrix–vector form; with this aim we introduce the matrices $\boldsymbol{\mathcal{R}}_p : \Omega \to \mathbb{R}^{N_h \times d}$ and $\widetilde{\boldsymbol{\mathcal{Z}}}_{PW}(\boldsymbol{k}) \in \mathbb{C}^{N_h \times d}$ reading, e.g. for the two–dimensional case $d = 2$:

$$\boldsymbol{\mathcal{R}}_p := \begin{bmatrix} \boldsymbol{R}_p & \boldsymbol{0} \\ \boldsymbol{0} & \boldsymbol{R}_p \end{bmatrix} \qquad \text{and} \qquad \widetilde{\boldsymbol{\mathcal{Z}}}_{PW}(\boldsymbol{k}) := \begin{bmatrix} \widetilde{\boldsymbol{Z}}_{PW}(\boldsymbol{k}) & \boldsymbol{0} \\ \boldsymbol{0} & \widetilde{\boldsymbol{Z}}_{PW}(\boldsymbol{k}) \end{bmatrix}, \tag{5.10}$$

where $\boldsymbol{R}_p : \Omega \to \mathbb{R}^{N_{bf}}$ is the vector of the NURBS basis functions $\boldsymbol{R}_p = \left(R_{1,p}, \ldots, R_{N_{bf},p}\right)^{\mathrm{T}}$. Then, the discrete harmonic plane wave $\widetilde{\boldsymbol{u}}_{PW,h}(t;\boldsymbol{k},\omega)$ reads:

$$\widetilde{\boldsymbol{u}}_{PW,h}(t;\boldsymbol{k},\omega) = \mathrm{e}^{-\imath\,\omega\,t}\, \boldsymbol{\mathcal{R}}_p^{\mathrm{T}}\, \widetilde{\boldsymbol{\mathcal{Z}}}_{PW}(\boldsymbol{k})\, \boldsymbol{\Psi} = \boldsymbol{\mathcal{R}}_p^{\mathrm{T}}\, \widetilde{\boldsymbol{U}}_{PW}(t;\boldsymbol{k},\omega). \tag{5.11}$$

where $\widetilde{\boldsymbol{U}}_{PW}(\boldsymbol{k},\omega) : \mathbb{R} \to \mathbb{C}^{N_h}$, being $\widetilde{\boldsymbol{U}}_{PW}(t;\boldsymbol{k},\omega) := \mathrm{e}^{-\imath\,\omega\,t}\, \widetilde{\boldsymbol{\mathcal{Z}}}_{PW}(\boldsymbol{k})\, \boldsymbol{\Psi}$.

According to the procedure proposed in [42], we replace the control variables $\widetilde{\boldsymbol{\mathcal{U}}}_{PW}(t;\boldsymbol{k},\omega)$ of the discrete harmonic plane wave $\widetilde{\boldsymbol{u}}_{PW,h}(t;\boldsymbol{k},\omega)$ into Eq. (5.7), thus obtaining:

$$\left(-\omega^2 \boldsymbol{\mathcal{M}} + \boldsymbol{\mathcal{K}}\right)\, \widetilde{\boldsymbol{\mathcal{Z}}}_{PW}(\boldsymbol{k})\, \boldsymbol{\Psi} = \boldsymbol{0}, \tag{5.12}$$

after having simplified the term $e^{-\imath\,\omega\,t}$. By pre–multiplying the previous equation by the matrix $\left(\widetilde{\boldsymbol{\mathcal{Z}}}_{PW}(\boldsymbol{k})\right)^{\mathrm{H}}$ corresponding to the transpose complex conjugate of $\widetilde{\boldsymbol{\mathcal{Z}}}_{PW}(\boldsymbol{k})$, we obtain the following d–dimensional generalized eigenvalue problem for a prescribed wave vector $\boldsymbol{k}$:

$$\text{find } \widetilde{\omega}_h(\boldsymbol{k}) \in \mathbb{R},\, \widetilde{\boldsymbol{\Psi}}_h(\boldsymbol{k}) \in \mathbb{R}^d \quad : \quad \widetilde{\boldsymbol{\mathcal{K}}}_{\widetilde{\boldsymbol{\mathcal{Z}}}_{PW}}(\boldsymbol{k})\, \widetilde{\boldsymbol{\Psi}}_h(\boldsymbol{k}) = \left(\widetilde{\omega}_h(\boldsymbol{k})\right)^2\, \widetilde{\boldsymbol{\mathcal{M}}}_{\widetilde{\boldsymbol{\mathcal{Z}}}_{PW}}(\boldsymbol{k})\, \widetilde{\boldsymbol{\Psi}}_h(\boldsymbol{k}), \tag{5.13}$$

where:

$$\widetilde{\boldsymbol{\mathcal{K}}}_{\widetilde{\boldsymbol{\mathcal{Z}}}_{PW}}(\boldsymbol{k}) := \left(\widetilde{\boldsymbol{\mathcal{Z}}}_{PW}(\boldsymbol{k})\right)^{\mathrm{H}}\, \boldsymbol{\mathcal{K}}\, \widetilde{\boldsymbol{\mathcal{Z}}}_{PW}(\boldsymbol{k}) \tag{5.14}$$

[2] The Gauss–Legendre quadrature formula used to approximate the integrals in the weak form (5.8) will be discussed in Sec. 5.3.

and

$$\widetilde{\boldsymbol{\mathcal{M}}}_{\widetilde{\boldsymbol{\mathcal{Z}}}_{PW}}(\boldsymbol{k}) := \left(\widetilde{\boldsymbol{\mathcal{Z}}}_{PW}(\boldsymbol{k})\right)^{\mathrm{H}} \boldsymbol{\mathcal{M}}\, \widetilde{\boldsymbol{\mathcal{Z}}}_{PW}(\boldsymbol{k}). \tag{5.15}$$

Following [42], one can show that the d eigenvalues $\widetilde{\omega}_h(\boldsymbol{k})$ are real.

By specializing to the two–dimensional case for which $d = 2$, we can associate the largest of the two eigenvalues, say $\widetilde{\omega}_{p,h}(\boldsymbol{k})$, to the discrete compressional wave (P–wave), while the smallest, say $\widetilde{\omega}_{s,h}(\boldsymbol{k})$, to the discrete shear wave (S–wave). Then, from the previous discrete angular frequencies $\widetilde{\omega}_{p,h}(\boldsymbol{k})$ and $\widetilde{\omega}_{s,h}(\boldsymbol{k})$ we compute the numerical wave velocities for a given $\boldsymbol{k}$:

$$\widetilde{c}_{p,h}(\boldsymbol{k}) := \frac{\widetilde{\omega}_{p,h}(\boldsymbol{k})}{\kappa} \qquad \text{and} \qquad \widetilde{c}_{s,h}(\boldsymbol{k}) := \frac{\widetilde{\omega}_{s,h}(\boldsymbol{k})}{\kappa}, \tag{5.16}$$

together with the corresponding wave velocity errors:

$$\widetilde{e}_p(\boldsymbol{k}) := \frac{\widetilde{c}_{p,h}(\boldsymbol{k})}{c_p} - 1 \qquad \text{and} \qquad \widetilde{e}_s(\boldsymbol{k}) := \frac{\widetilde{c}_{s,h}(\boldsymbol{k})}{c_s} - 1; \tag{5.17}$$

from the previous errors we introduce the corresponding relative errors, often used in studying the effect of the wave direction (i.e. the angle θ), reading:

$$\widehat{\widetilde{e}}_p(\boldsymbol{k}) := \widetilde{e}_p(\boldsymbol{k}) + 1 \qquad \text{and} \qquad \widehat{\widetilde{e}}_s(\boldsymbol{k}) := \widetilde{e}_s(\boldsymbol{k}) + 1. \tag{5.18}$$

5.3 Dispersion analysis for NURBS

We aim at performing the numerical dispersion analysis following the procedure outlined in Sec. 5.2 with NURBS basis functions of different degrees p and different regularity, namely C^α–continuous in Ω for some $\alpha = 0, \dots, p-1$ as discussed in Sec. 3. Specifically, we are interested in performing such analysis when considering the same number of NURBS basis functions in each parametric direction per wave length. We remark that this represents an adaptation to the NURBS context of the numerical *grid* dispersion analysis performed with Finite Elements ([22, 23, 28, 34, 39]) or Spectral methods ([5, 42]) for which basis functions are interpolatory at the grid nodes.

Let us specifically consider the two–dimensional case for which $d = 2$ with the computational domain $\Omega = (0,1)^2$ and assume that the wave vector $\boldsymbol{k}$ is in the form:

$$\boldsymbol{k} = 2\pi\, k\, \left(\cos(\theta), \sin(\theta)\right)^{\mathrm{T}}, \tag{5.19}$$

with $k > 0$ the circular wavelength and $\theta \in [0, 2\pi)$; we notice that when the angle θ is expressed in degrees, it is indicated as ϑ ($[^\circ]$) reading $\vartheta = \theta\, \dfrac{180^\circ}{\pi}$. We recall that bivariate NURBS basis functions are built by applying the tensor product rule to the univariate basis functions, which we assume to possess the same degree p and global continuity α along all the parametric directions (i.e. built from the same knot vectors Ξ along both the parametric directions). By recalling the notation of Sec. 3.1, we indicate with $N_{bf} = n^2$ the total number of basis functions, where n is the number of basis functions along the single parametric direction, which we fix a priori. We define the number of NURBS basis functions in each parametric direction per wave length, say G, and its inverse measuring the wave length per resolution, say H, as:

$$G := \frac{n}{k} \qquad \text{and} \qquad H := \frac{k}{n}. \tag{5.20}$$

Since we are aiming at comparing the numerical dispersion for NURBS basis functions of different regularity, namely C^α–continuous for $\alpha = 0, \ldots, p-1$, for fixed values of H, that is with a fixed number of univariate basis functions n for a prescribed wave length k, we need to built such basis functions from knot vectors possessing a different number of non–zero elements n_{el}, say $n_{el,\alpha}$. According to the formula (3.3), we have:

$$n_{el,\alpha} = \lceil \widetilde{n}_{el,\alpha} \rceil , \qquad \text{with } \widetilde{n}_{el,\alpha} := \frac{n-\alpha-1}{p-\alpha} \qquad \text{for } \alpha = 0, \ldots, p-1, \tag{5.21}$$

for a prescribed value of univariate basis functions $n > p+1$ and degree $p \geq 1$ ([3]).

On the other side, since we are operating in the Galerkin framework, the numerical dispersion analysis stemming from the solution of the generalized eigenvalue problem (5.13), involves the use of quadrature formulas for approximating the integrals related to the assembly of the matrices $\boldsymbol{\mathcal{M}}$ and $\boldsymbol{\mathcal{K}}$ of Eq. (5.7), as well as to the computation of the control variables $\widetilde{\boldsymbol{Z}}_{PW}(\boldsymbol{k})$ of L^2–projection problem (5.8). When considering B–splines basis functions, the standard Gauss–Legendre quadrature formula (4.8) with $r = p+1$ quadrature nodes per element along each parametric direction ensures the exact assembly of the matrices $\boldsymbol{\mathcal{M}}$ and $\boldsymbol{\mathcal{K}}$, while this is not the case of the integrals involved in the problem (5.8), since the harmonic plane wave function $z_{PW}(\boldsymbol{k})$ is not of polynomial type. Indeed, the assembly of the matrices $\boldsymbol{\mathcal{M}}$ and $\boldsymbol{\mathcal{K}}$ with the standard Gauss–Legendre formula with $r = p+1$ is exact regardless the regularity $\alpha = 0, \ldots, p-1$ of the B–splines basis functions. Conversely, the computation of the control variables $\widetilde{\boldsymbol{Z}}_{PW}(\boldsymbol{k})$ for the harmonic plane waves is sensitive to the regularity of the B–splines basis functions α, since a different total number of quadrature nodes per parametric direction, say $n_{qn,\alpha}$, is used, being $n_{qn,\alpha} = r\, n_{el,\alpha}$ for $\alpha = 0, \ldots, p-1$. It follows that if we aim at comparing the numerical dispersion obtained by B–splines basis functions of different regularity $\alpha = 0, \ldots, p-1$ under the same conditions, namely the same value of the parameter G of Eq. (5.20), we also have to ensure that the error associated to the numerical quadrature is "sufficiently" small; the latter goal can be achieved by considering the same total number of quadrature nodes per wave length, say Q, defined as:

$$Q := \frac{n_{nq}}{k}, \tag{5.22}$$

where n_{qn} is the prescribed number of quadrature nodes along each parametric direction and k is the circular wavelength of Eq. (5.19). Since the number of elements $n_{el,\alpha}$ increases when the regularity of the B–splines basis functions decreases, i.e. for $\alpha = p-1, \ldots, 0$, according to the formula (5.21), and with a prescribed n, we set $n_{qn} = r_{p-1}\, n_{el,p-1}$, where $r_{p-1} = r = p+1$ for the standard Gauss–Legendre quadrature formula. By enforcing $n_{qn,\alpha} := r_\alpha\, n_{el,\alpha} \geq n_{qn}$ for all $\alpha = 0, \ldots, p-2$, we obtain from Eqs. (3.3) and (5.21) that the number of Gauss–Legendre quadrature nodes per mesh element r_α varies for C^α–continuous B–splines basis functions as:

$$r_\alpha = \lceil \widetilde{r}_\alpha \rceil , \qquad \text{with } \widetilde{r}_\alpha := \frac{n_{nq}}{\widetilde{n}_{el,\alpha}} = r\,(p-\alpha)\frac{n-p}{n-\alpha-1} \qquad \text{for } \alpha = 0, \ldots, p-1. \tag{5.23}$$

We remark that according to the previous formula, the total number of Gauss–Legendre quadrature nodes per mesh element r_α is larger for smaller values of α; in this manner, the total number of quadrature nodes per wave length Q (see Eq. (5.22)) is slightly biased in favor of C^0–continuous basis functions with respect to basis functions which are globally C^{p-1}–continuous, i.e. $n_{qn,0} \widetilde{\geq} n_{qn,p-1}$ ([4]).

[3] For example for $n = 10$ and $p = 3$, we have $n_{el,\alpha} = 3$, 4, and 7, for $\alpha = 0$, 1, and 2, respectively.

[4] For example for $n = 10$ and $p = 3$, we have $r_\alpha = 10$, 7, and 4 and $n_{qn,\alpha} = 30$, 28, and 28, for $\alpha = 0$, 1, and 2, respectively.

We use the above Gauss–Legendre quadrature formulas also when considering NURBS basis functions, even if in this case the assembly of the matrices $\boldsymbol{\mathcal{M}}$ and $\boldsymbol{\mathcal{K}}$ of Eq. (5.7) also involves some numerical quadrature errors other than the computation of the control variables $\widetilde{\boldsymbol{Z}}_{PW}(\boldsymbol{k})$ in Eq. (5.8) as for B–splines basis functions.

5.4 Dispersion analysis: numerical results

We propose and discuss some numerical results for the dispersion analysis according to the generalized eigenvalue problem outlined in Sec. 5.2. We consider both the cases of B–splines and NURBS basis functions by comparing different polynomial degrees p and regularity $\alpha = 0$ and $p-1$, i.e. basis functions which are either C^0– or C^{p-1}–continuous. We propose a comparison both in terms of the phase velocity errors $\widetilde{e}_p(\boldsymbol{k})$ and $\widetilde{e}_s(\boldsymbol{k})$ of Eq. (5.17) associated to the compressional and shear waves (P– and S–waves) vs. the parameter H of Eq. (5.20), i.e. the resolution per wavelength. We also discuss the influence of the Poisson's ratio ν on the numerical dispersion analysis.

Following the discussion about the Gauss–Legendre quadrature formulas in Sec. 5.3, we remark that the use of the enhanced quadrature rule r_α of Eq. (5.23) for "small" values of the parameter H of Eq. (5.20) does not significantly affect the results of the numerical dispersion analysis obtained for $r = p+1$ regardless of the regularity α of the NURBS basis functions. Conversely, for "large" values of H, e.g. $H \simeq 0.25 - 0.5$ the numerical errors associated to basis functions of low regularity are generally very sensitive to the choice of the number of quadrature nodes per mesh element. Therefore, all the numerical results presented in this section are obtained with the Gauss–Legendre quadrature rule r_α provided in Eq. (5.23).

For the numerical tests considered in this section, we set the density $\rho = 2 \cdot 10^3\, kg/m^3$ and the exact compressional wave (P–wave) velocity $c_p = 3 \cdot 10^3\, m/s$; the remaining elastic parameters are computed from ρ, c_p, and the Poisson's ratio ν by means of Eq. (2.2). Specifically, the exact shear wave (S–wave) velocity is determined as $c_s = c_p \sqrt{\dfrac{1-2\nu}{2(1-\nu)}}$; e.g. we have $c_s = 2 \cdot 10^3\, m/s$ and $c_s = 1.225 \cdot 10^3\, m/s$ for $\nu = 0.1$ and $\nu = 0.4$, respectively. We consider both B–splines and NURBS basis functions with a fixed number of univariate basis functions equal to $n = 25$ regardless of their polynomial degree $p = 1, 2, 3$, and 4 and their global C^0– or C^{p-1}–continuity; the resolution per wave length determined by the parameter H is varied by changing the modulus of the circular wavelength k (see Eq. (5.19)).

B–splines basis functions

We start our numerical dispersion analysis for B–splines basis functions by comparing the phase errors $\widetilde{e}_p(\boldsymbol{k})$ and $\widetilde{e}_s(\boldsymbol{k})$ associated to the P– and S–waves velocities of Eq. (5.17), respectively, vs. H. We consider different values of the Poisson's ratio $\nu = 0.1$ and 0.4, with the angles $\vartheta = 0^\circ$ and 45° for the direction of the wave vector $\boldsymbol{k}$ of Eq. (5.19). In Figs. 3–6 we report the results obtained for B–splines basis functions of polynomial degrees $p = 1, 2, 3$, and 4 and globally C^α-continuous for $\alpha = 0$ and $\alpha = p-1$. We notice that the errors corresponding to basis functions of the maximum regularity, i.e. globally C^{p-1}–continuous, are generally smaller than their C^0–continuous counterpart of the same polynomial degree p, also for relatively large values of the parameter H; this is evident for example in the approximation of the shear S–wave velocity for $\vartheta = 45^\circ$ for the values of the Poisson's ratio $\nu = 0.1$ and 0.4 in Figs. 4(c)–(d) and 6(c)–(d), for which we report a significantly smaller error $\widetilde{e}_s(\boldsymbol{k})$ with globally C^{p-1}–continuous basis functions. As for example,

B–splines: $\nu = 0.1$ and $\vartheta = 0^\circ$ $(\theta = 0)$.

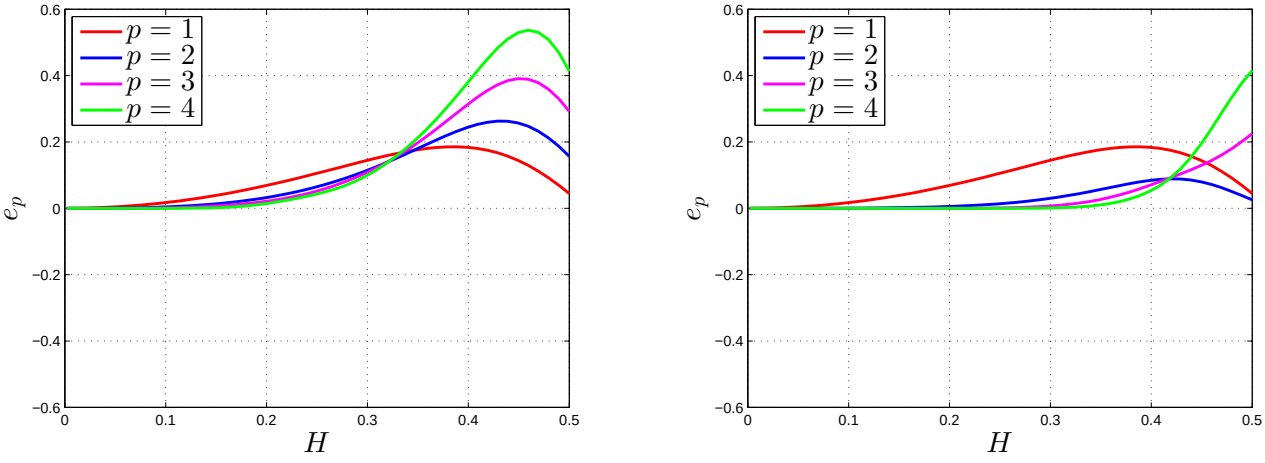

(a) $\widetilde{e}_p(\boldsymbol{k})$ vs. H for $\alpha = 0$

(b) $\widetilde{e}_p(\boldsymbol{k})$ vs. H for $\alpha = p - 1$

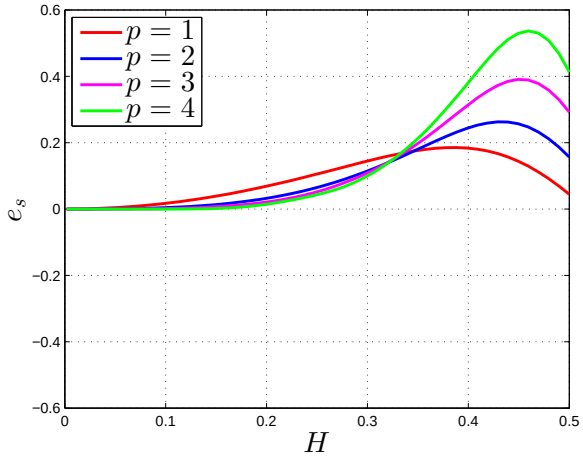

(c) $\widetilde{e}_s(\boldsymbol{k})$ vs. H for $\alpha = 0$

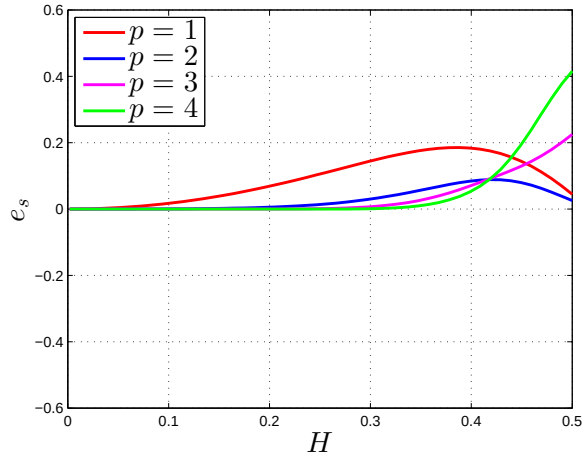

(d) $\widetilde{e}_s(\boldsymbol{k})$ vs. H for $\alpha = p - 1$

Figure 3: P– and S–waves velocity errors $\widetilde{e}_p(\boldsymbol{k})$ (top) and $\widetilde{e}_s(\boldsymbol{k})$ (bottom) vs. H for $\nu = 0.1$, $\vartheta = 0^\circ$ $(\theta = 0)$, and $p = 1, 2, 3, 4$; B–splines basis functions globally C^α–continuous with $\alpha = 0$ (left) and $\alpha = p - 1$ (right).

we observe from Figs. 6(c)–(d) that the values of the computed S–wave velocities $\widetilde{c}_{s,h}(\boldsymbol{k})$ obtained with B–splines basis functions of polynomial degree $p = 2$ for $H = 0.3$ are about the 30% and 10% larger than the exact one $c_s(\boldsymbol{k})$ when considering basis functions which are C^0– and C^1–continuous, respectively; similar results are obtained for $p = 3$ and 4. We also observe that the superiority of C^{p-1}–continuous basis versus the C^0–continuous ones is not affected by the choice of the Poisson's ratio ν and the angle ϑ of the wave vector $\boldsymbol{k}$; moreover, from Figs. 4 and 6 we observe that the errors obtained with C^0–continuous basis functions are more sensitive to the choice of the Poisson's ratio ν with respect to B–splines basis functions C^{p-1}–continuous, as clearly highlighted for the errors $\widetilde{e}_s(\boldsymbol{k})$.

B–splines: $\nu = 0.1$ and $\vartheta = 45^\circ$ ($\theta = \pi/4$).

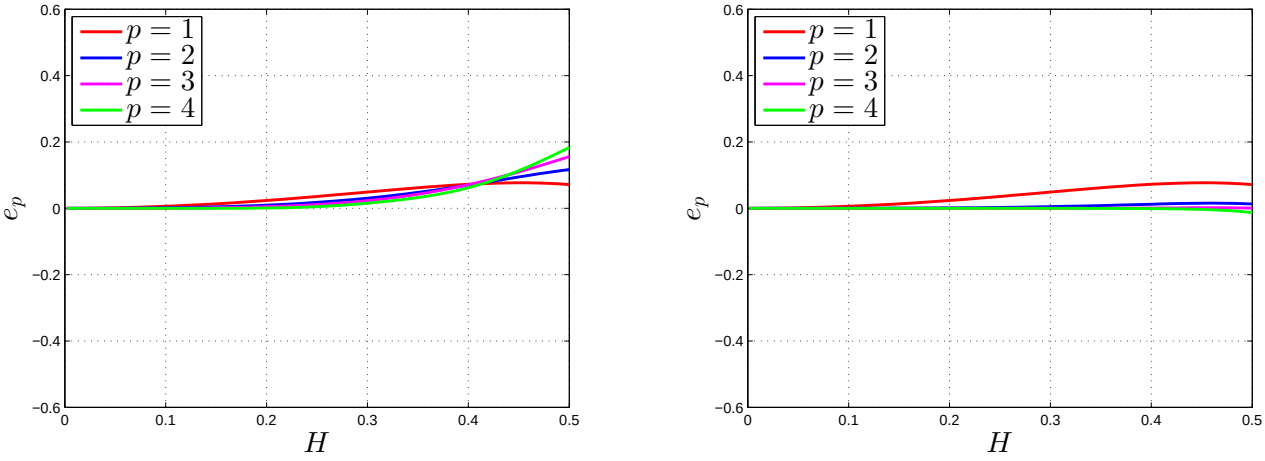

(a) $\widetilde{e}_p(\boldsymbol{k})$ vs. H for $\alpha = 0$

(b) $\widetilde{e}_p(\boldsymbol{k})$ vs. H for $\alpha = p - 1$

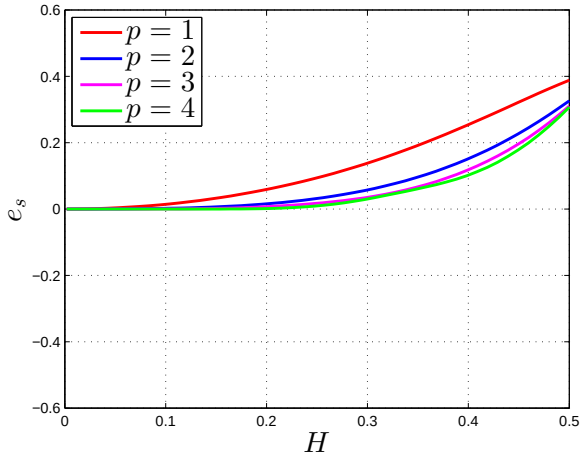

(c) $\widetilde{e}_s(\boldsymbol{k})$ vs. H for $\alpha = 0$

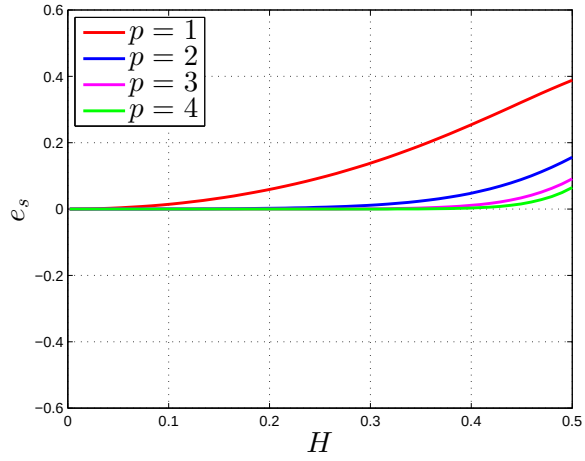

(d) $\widetilde{e}_s(\boldsymbol{k})$ vs. H for $\alpha = p - 1$

Figure 4: P– and S–waves velocity errors $\widetilde{e}_p(\boldsymbol{k})$ (top) and $\widetilde{e}_s(\boldsymbol{k})$ (bottom) vs. H for $\nu = 0.1$, $\vartheta = 45^\circ$ ($\theta = \pi/4$), and $p = 1, 2, 3, 4$; B–splines basis functions globally C^α–continuous with $\alpha = 0$ (left) and $\alpha = p - 1$ (right).

In Figs. 7–10 we compare the relative P– and S–waves velocity errors $\widehat{e}_p(\boldsymbol{k})$ and $\widehat{e}_s(\boldsymbol{k})$ of Eq. (5.18) by means of the so–called anisotropic curves, that is the representation of such errors in polar coordinates for different wave directions $\boldsymbol{k}$ obtained by changing the angle ϑ (or θ) in Eq. (5.19). In this comparison we consider the results obtained with globally C^0– and C^{p-1}–continuous B–splines basis functions of polynomial degrees $p = 1, 2, 3$, and 4 with $\nu = 0.1$ and 0.4; such results are obtained by setting the number of control variables per wave length $G = 4$, or equivalently $H = 0.25$ according to the definitions (5.20). As we can observe already from Fig. 7, both the numerical P– and S–wave velocities overestimate the exact ones, with the maximum errors occurring at $\vartheta = 0^\circ$ for the P–wave, while at $\vartheta = 45^\circ$ for the S–wave. Also, we observe that the

B–splines: $\nu = 0.4$ and $\vartheta = 0^\circ$ ($\theta = 0$).

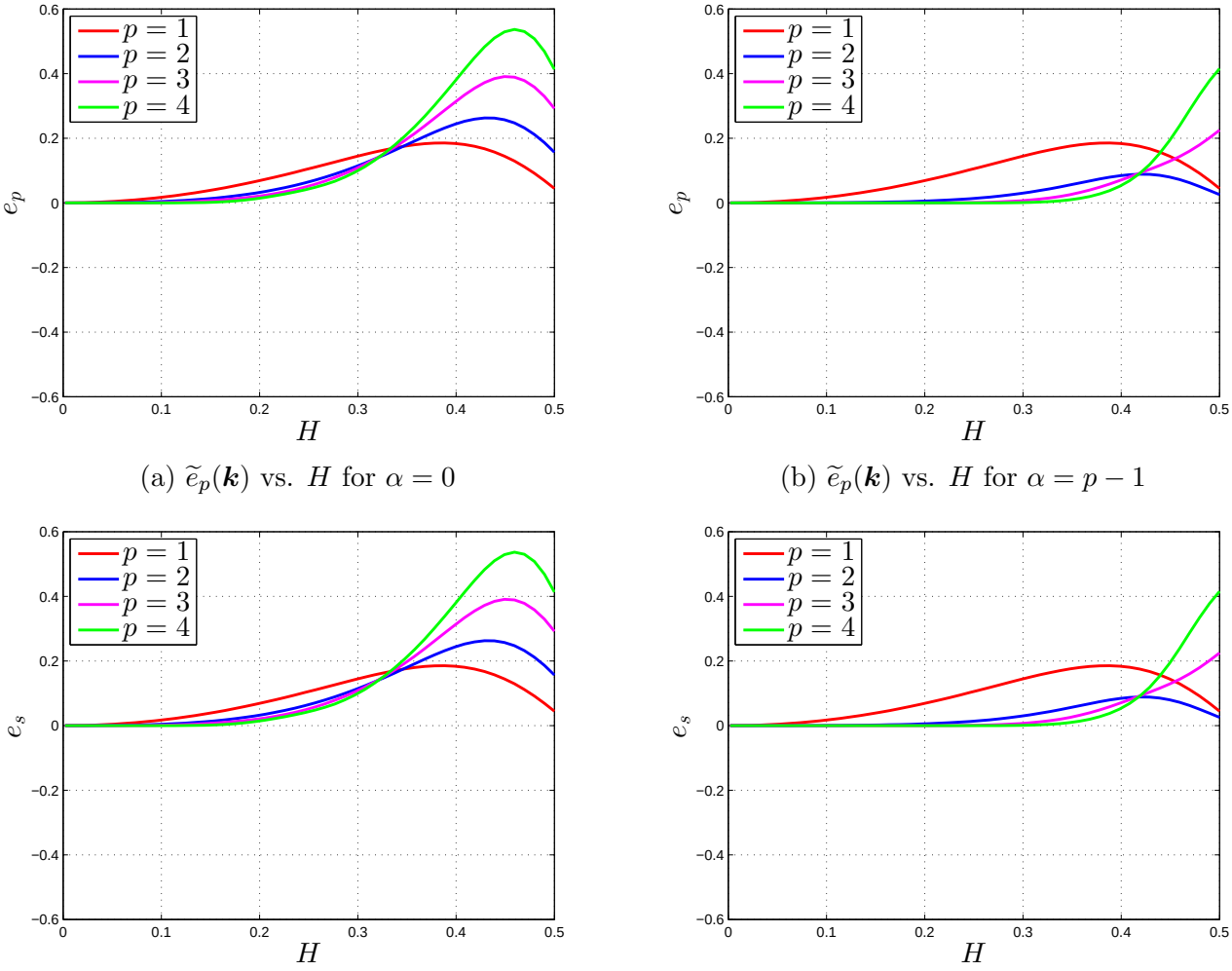

(a) $\widetilde{e}_p(\boldsymbol{k})$ vs. H for $\alpha = 0$

(b) $\widetilde{e}_p(\boldsymbol{k})$ vs. H for $\alpha = p - 1$

(c) $\widetilde{e}_s(\boldsymbol{k})$ vs. H for $\alpha = 0$

(d) $\widetilde{e}_s(\boldsymbol{k})$ vs. H for $\alpha = p - 1$

Figure 5: P– and S–waves velocity errors $\widetilde{e}_p(\boldsymbol{k})$ (top) and $\widetilde{e}_s(\boldsymbol{k})$ (bottom) vs. H for $\nu = 0.4$, $\vartheta = 0^\circ$ ($\theta = 0$), and $p = 1, 2, 3, 4$; B–splines basis functions globally C^α–continuous with $\alpha = 0$ (left) and $\alpha = p - 1$ (right).

error associated to the S–wave velocity is very sensitive to the chosen Poisson's ratio, conversely to the P–wave velocity error for which the anisotropic curves qualitatively overlap. As evident from all the Figs. 8–10, the curves obtained by means of globally C^{p-1}–continuous basis functions outperform the corresponding ones obtained with the corresponding globally C^0–continuous ones.

B–splines: $\nu = 0.4$ and $\vartheta = 45^\circ$ ($\theta = \pi/4$).

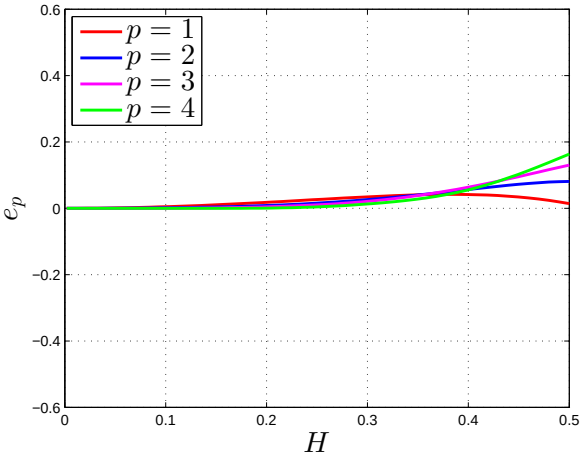

(a) $\widetilde{e}_p(\boldsymbol{k})$ vs. H for $\alpha = 0$

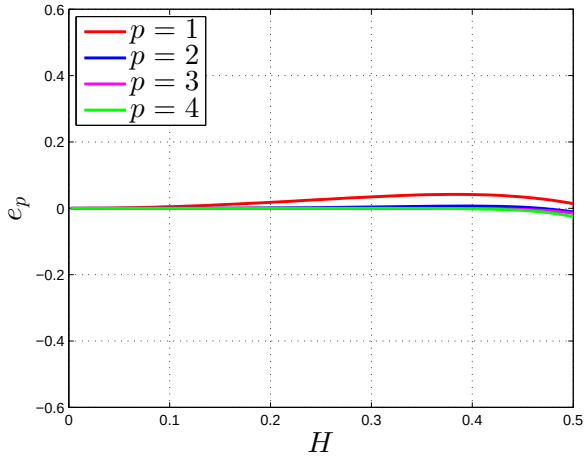

(b) $\widetilde{e}_p(\boldsymbol{k})$ vs. H for $\alpha = p - 1$

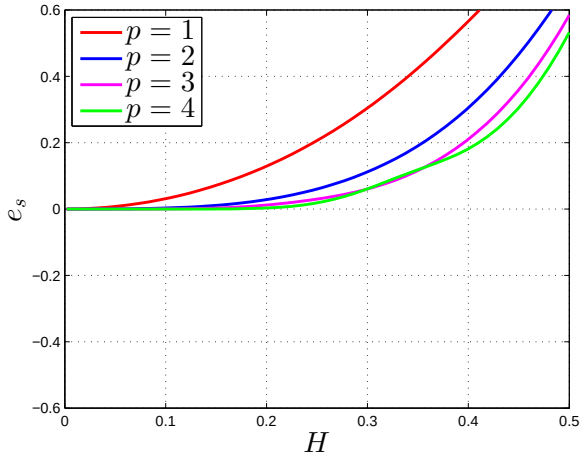

(c) $\widetilde{e}_s(\boldsymbol{k})$ vs. H for $\alpha = 0$

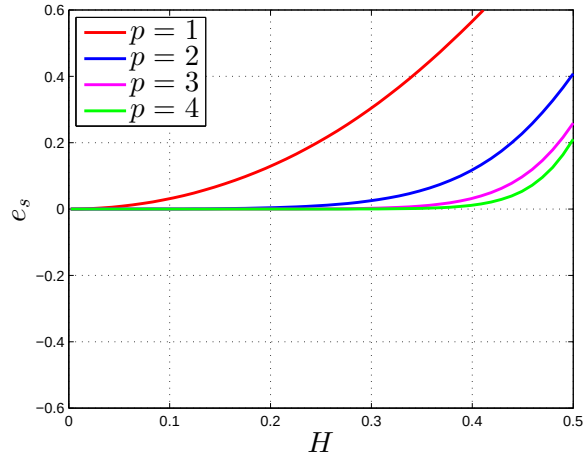

(d) $\widetilde{e}_s(\boldsymbol{k})$ vs. H for $\alpha = p - 1$

Figure 6: P– and S–waves velocity errors $\widetilde{e}_p(\boldsymbol{k})$ (top) and $\widetilde{e}_s(\boldsymbol{k})$ (bottom) vs. H for $\nu = 0.4$, $\theta = 45^\circ$ ($\theta = \pi/4$), and $p = 1, 2, 3, 4$; B–splines basis functions globally C^α–continuous with $\alpha = 0$ (left) and $\alpha = p - 1$ (right).

B–splines: $p = 1$.

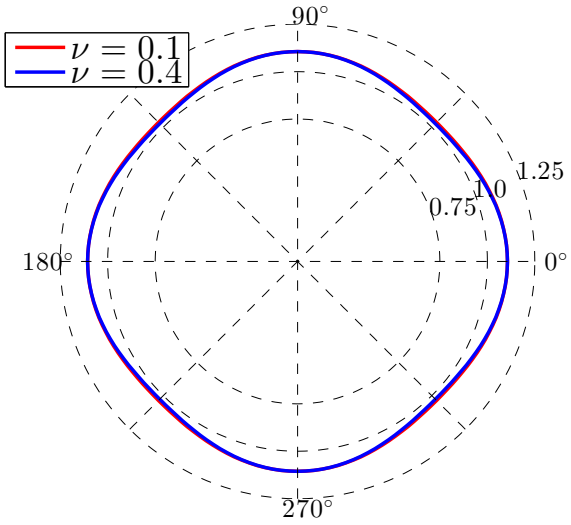

(a) $\widehat{e}_p(\boldsymbol{k})$ vs. ϑ

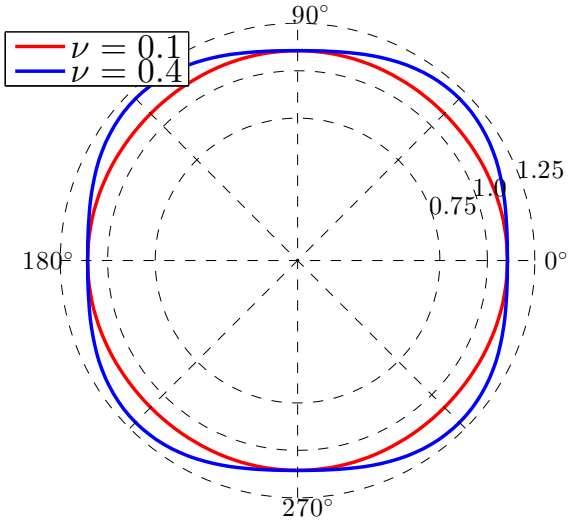

(b) $\widehat{e}_s(\boldsymbol{k})$ vs. ϑ

Figure 7: P– and S–waves velocity relative errors $\widehat{e}_p(\boldsymbol{k})$ (top) and $\widehat{e}_s(\boldsymbol{k})$ (bottom) vs. $\vartheta \in [0, 360°)$ ($\theta \in [0, 2\pi)$) in polar coordinates, obtained with $G = 4$ ($H = 0.25$), for $\nu = 0.1$ (blue) and $\nu = 0.4$ (red); B–splines basis functions of degree $p = 1$ and globally C^0–continuous.

B–splines: $p = 2$.

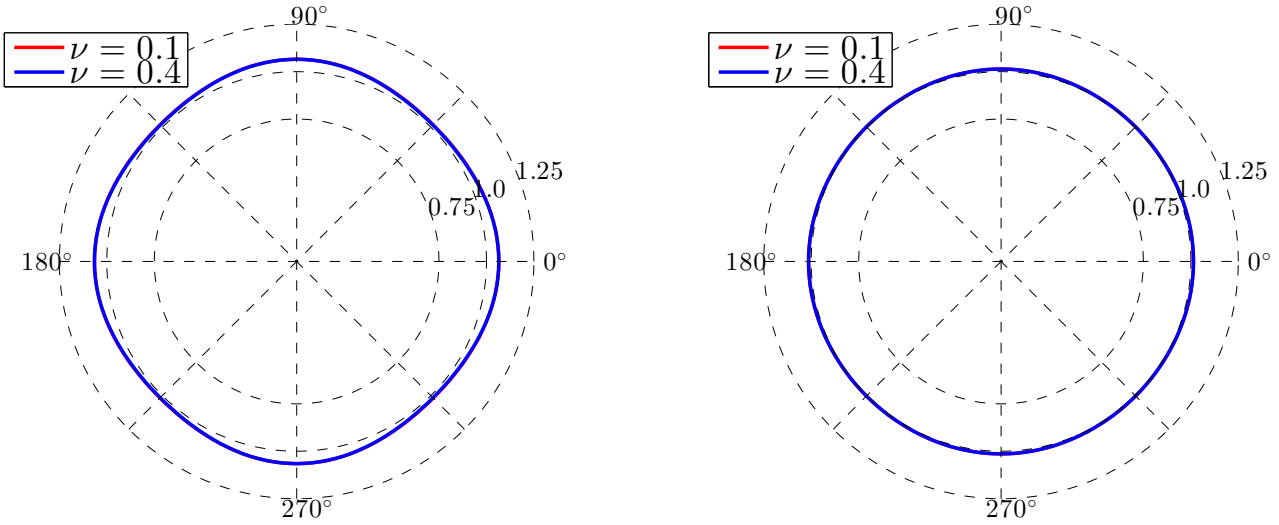

(a) $\widehat{e}_p(\boldsymbol{k})$ vs. ϑ for $\alpha = 0$

(b) $\widehat{e}_p(\boldsymbol{k})$ vs. ϑ for $\alpha = 1$

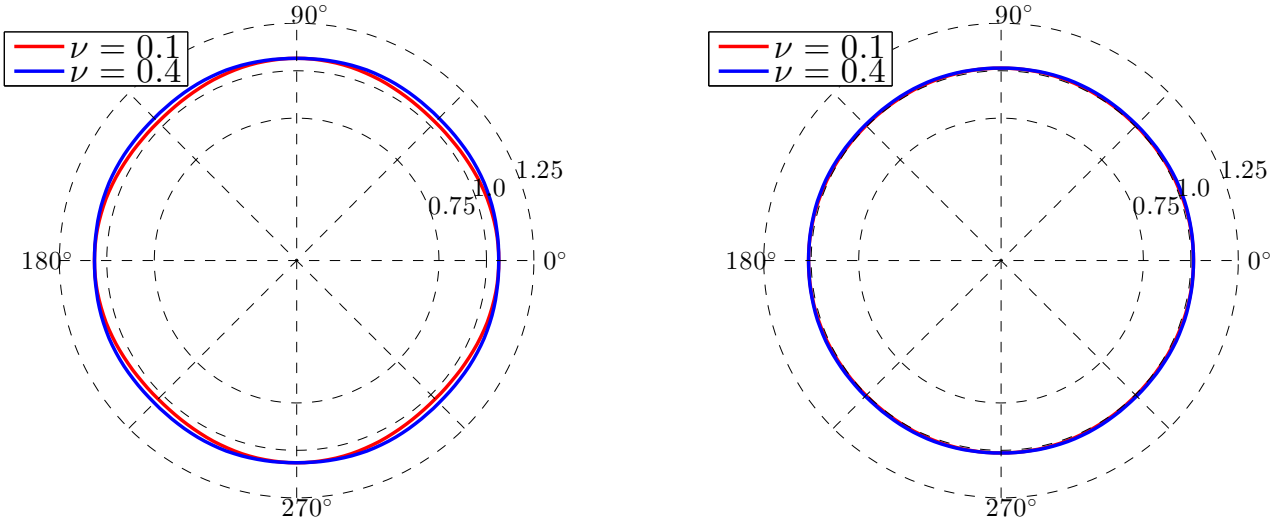

(c) $\widehat{e}_s(\boldsymbol{k})$ vs. ϑ for $\alpha = 0$

(d) $\widehat{e}_s(\boldsymbol{k})$ vs. ϑ for $\alpha = 1$

Figure 8: P– and S–waves velocity relative errors $\widehat{e}_p(\boldsymbol{k})$ (top) and $\widehat{e}_s(\boldsymbol{k})$ (bottom) vs. $\vartheta \in [0, 360°)$ ($\theta \in [0, 2\pi)$) in polar coordinates, obtained with $G = 4$ ($H = 0.25$), for $\nu = 0.1$ (blue) and $\nu = 0.4$ (red); B–splines basis functions of degree $p = 2$ and globally C^α–continuous with $\alpha = 0$ (left) and $\alpha = p - 1 = 1$ (right).

B–splines: $p = 3$.

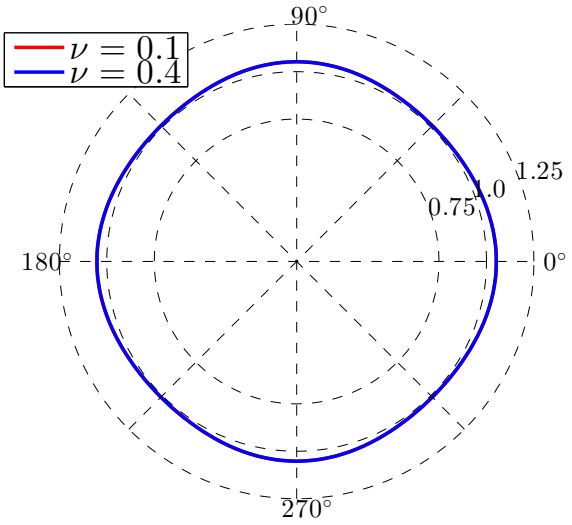

(a) $\widehat{e}_p(\boldsymbol{k})$ vs. ϑ for $\alpha = 0$

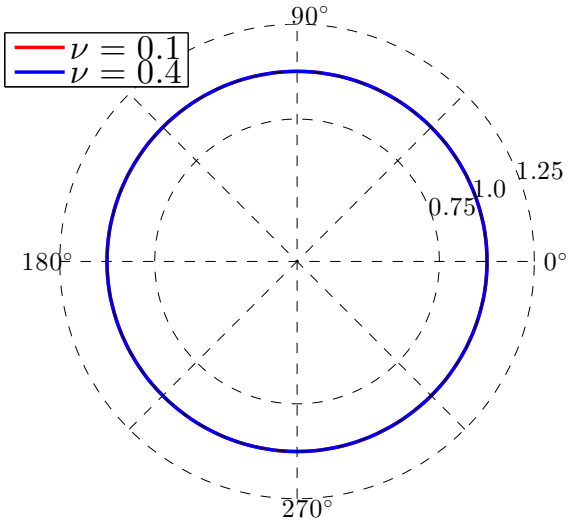

(b) $\widehat{e}_p(\boldsymbol{k})$ vs. ϑ for $\alpha = 2$

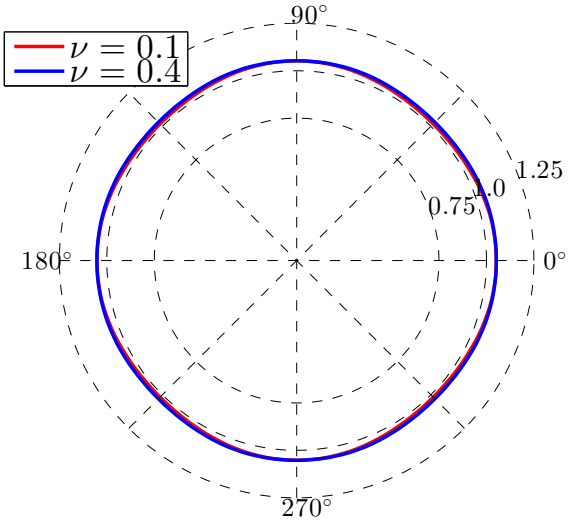

(c) $\widehat{e}_s(\boldsymbol{k})$ vs. ϑ for $\alpha = 0$

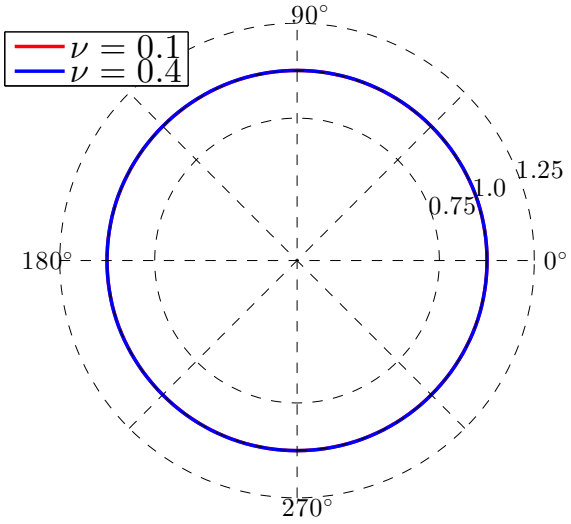

(d) $\widehat{e}_s(\boldsymbol{k})$ vs. ϑ for $\alpha = 2$

Figure 9: P– and S–waves velocity relative errors $\widehat{e}_p(\boldsymbol{k})$ (top) and $\widehat{e}_s(\boldsymbol{k})$ (bottom) vs. $\vartheta \in [0, 360°)$ ($\theta \in [0, 2\pi)$) in polar coordinates, obtained with $G = 4$ ($H = 0.25$), for $\nu = 0.1$ (blue) and $\nu = 0.4$ (red); B–splines basis functions of degree $p = 3$ and globally C^α–continuous with $\alpha = 0$ (left) and $\alpha = p - 1 = 2$ (right).

B–splines: $p = 4$.

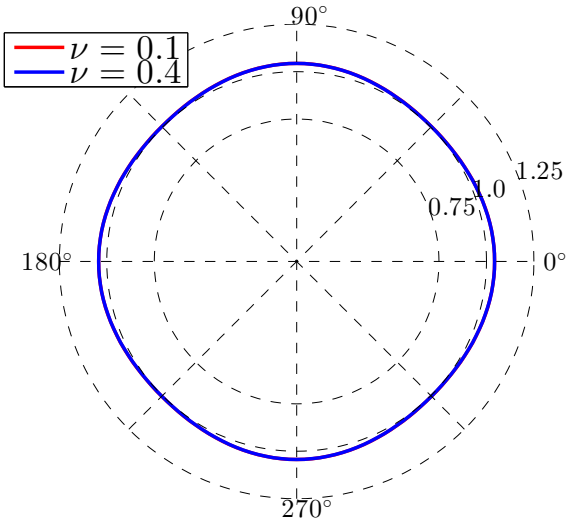

(a) $\widehat{e}_p(\boldsymbol{k})$ vs. ϑ for $\alpha = 0$

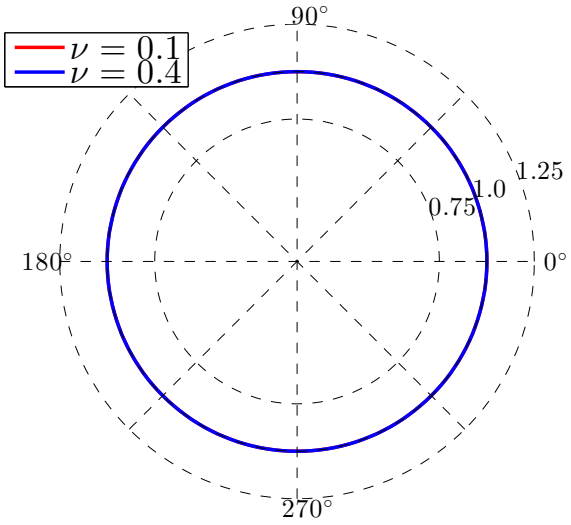

(b) $\widehat{e}_p(\boldsymbol{k})$ vs. ϑ for $\alpha = 3$

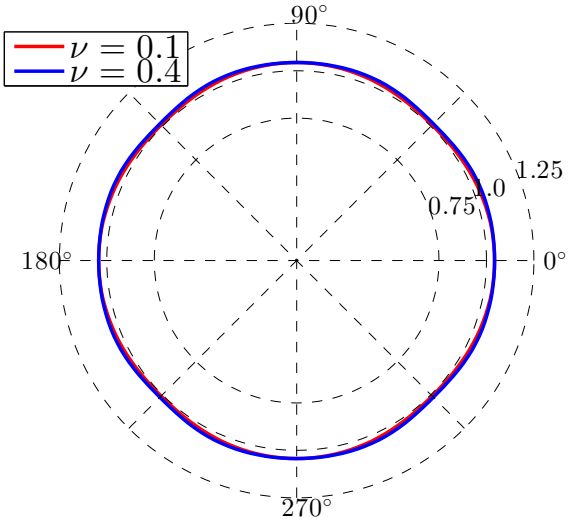

(c) $\widehat{e}_s(\boldsymbol{k})$ vs. ϑ for $\alpha = 0$

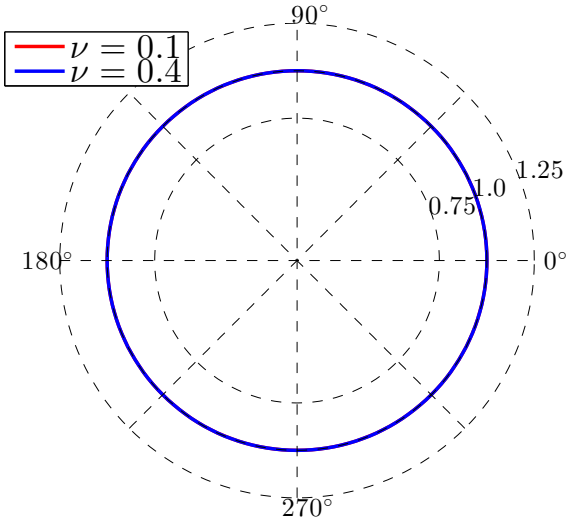

(d) $\widehat{e}_s(\boldsymbol{k})$ vs. ϑ for $\alpha = 3$

Figure 10: P– and S–waves velocity relative errors $\widehat{e}_p(\boldsymbol{k})$ (top) and $\widehat{e}_s(\boldsymbol{k})$ (bottom) vs. $\vartheta \in [0, 360°)$ ($\theta \in [0, 2\pi)$) in polar coordinates, obtained with $G = 4$ ($H = 0.25$), for $\nu = 0.1$ (blue) and $\nu = 0.4$ (red); B–splines basis functions of degree $p = 4$ and globally C^α–continuous with $\alpha = 0$ (left) and $\alpha = p - 1 = 3$ (right).

NURBS: $\nu = 0.1$ and $\vartheta = 0^\circ$ ($\theta = 0$).

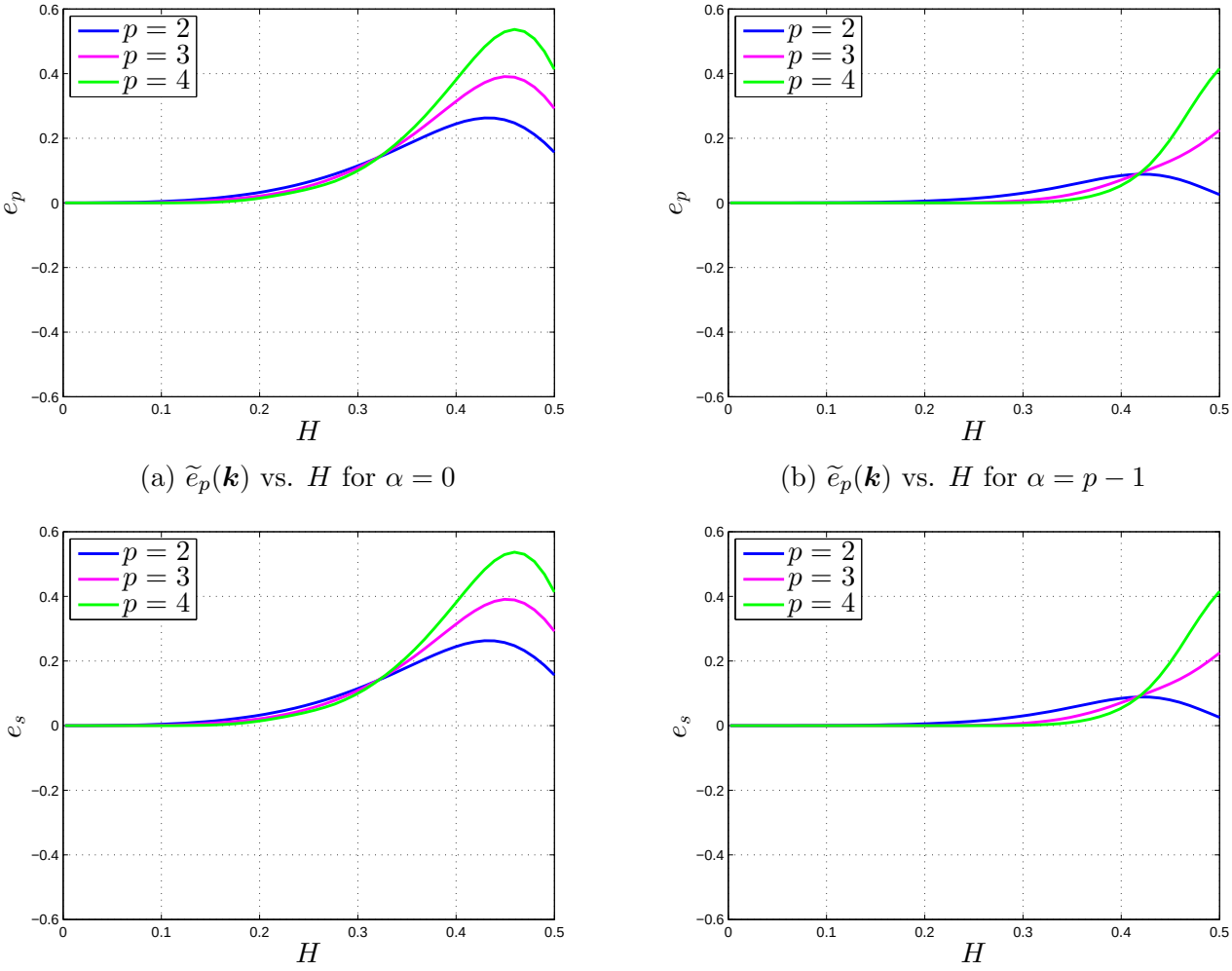

(a) $\widetilde{e}_p(\boldsymbol{k})$ vs. H for $\alpha = 0$

(b) $\widetilde{e}_p(\boldsymbol{k})$ vs. H for $\alpha = p - 1$

(c) $\widetilde{e}_s(\boldsymbol{k})$ vs. H for $\alpha = 0$

(d) $\widetilde{e}_s(\boldsymbol{k})$ vs. H for $\alpha = p - 1$

Figure 11: P– and S–waves velocity errors $\widetilde{e}_p(\boldsymbol{k})$ (top) and $\widetilde{e}_s(\boldsymbol{k})$ (bottom) vs. H for $\nu = 0.4$, $\vartheta = 0^\circ$ ($\theta = 0$), and $p = 2, 3, 4$; NURBS basis functions globally C^α–continuous with $\alpha = 0$ (left) and $\alpha = p - 1$ (right).

NURBS basis functions

As done for B–splines basis functions, we perform the same dispersion analysis for NURBS basis functions. As for example, we consider bivariate NURBS basis functions obtained by the application of the p– or k–refinement procedures (see Sec. 3.2 and [18]), depending on the desired regularity of the basis functions, starting from a reference basis. The latter is determined for the polynomial degree $p = 2$ from the knot vector $\Xi = \{0, 0, 0, 1, 1, 1\}$ along both the parametric directions, but weights $w_1 = w_3 = 1$ and $w_2 = 1/2$ only along the first parametric direction, being all unitary along the other; in this manner, we obtain NURBS basis functions which are not symmetric along both the parametric directions. With the same data considered for the B–splines basis functions, we report in Figs. 11 and 12 the errors $\widetilde{e}_p(\boldsymbol{k})$ and $\widetilde{e}_s(\boldsymbol{k})$ vs. H obtained for $p = 2, 3$, and 4 and

NURBS: $\nu = 0.1$ and $\vartheta = 45^\circ$ ($\theta = \pi/4$).

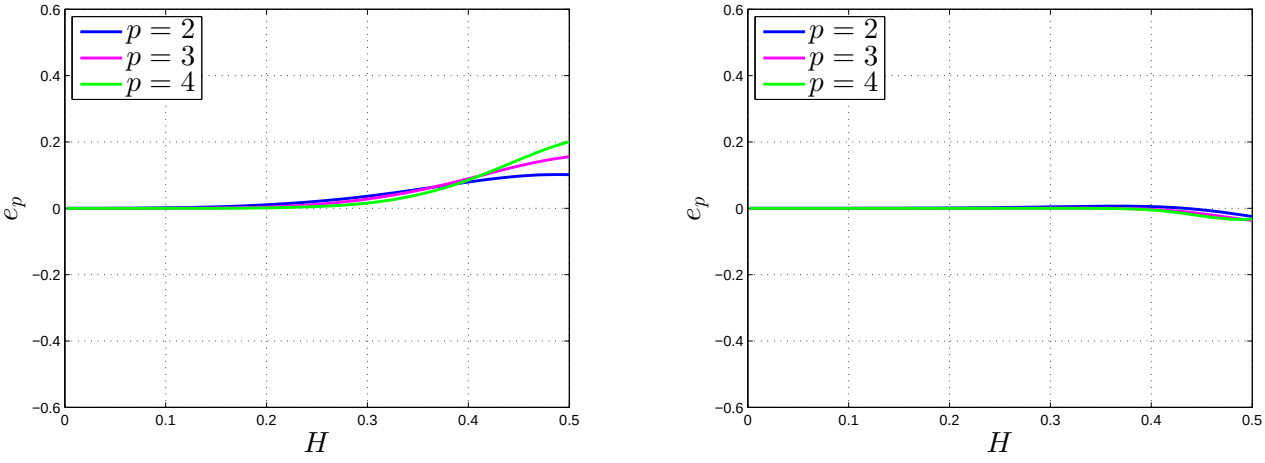

(a) $\widetilde{e}_p(\boldsymbol{k})$ vs. H for $\alpha = 0$

(b) $\widetilde{e}_p(\boldsymbol{k})$ vs. H for $\alpha = p - 1$

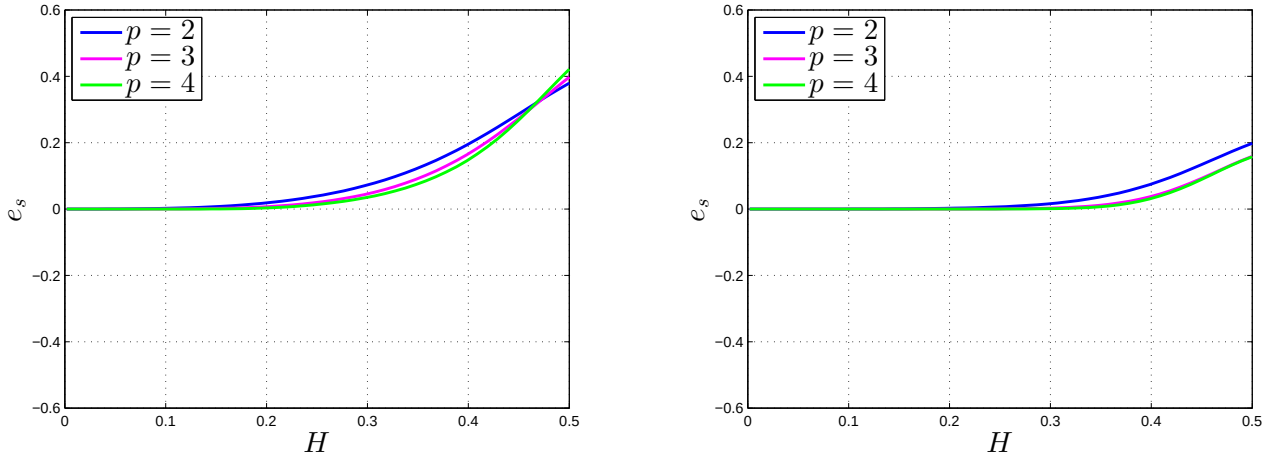

(c) $\widetilde{e}_s(\boldsymbol{k})$ vs. H for $\alpha = 0$

(d) $\widetilde{e}_s(\boldsymbol{k})$ vs. H for $\alpha = p - 1$

Figure 12: P– and S–waves velocity errors $\widetilde{e}_p(\boldsymbol{k})$ (top) and $\widetilde{e}_s(\boldsymbol{k})$ (bottom) vs. H for $\nu = 0.4$, $\vartheta = 45^\circ$ ($\theta = \pi/4$), and $p = 2, 3, 4$; NURBS basis functions globally C^α–continuous with $\alpha = 0$ (left) and $\alpha = p - 1$ (right).

$\nu = 0.1$ with the angles of the wave vector $\vartheta = 0^\circ$ and 45°, respectively. We notice that the results qualitatively resemble those obtained in Figs. 3 and 4. In particular, the same considerations about the superiority of globally C^{p-1}–continuous basis functions still hold.

In Fig. 13 we report the anisotropic curves obtained with the globally C^0– and C^1–continuous NURBS basis functions described previously; we consider both the cases of Poisson's ratio $\nu = 0.1$ and 0.4. Once again, we remark the superiority of the smooth basis with respect to the continuous ones. We remark that the anisotropic curves are not any longer symmetric along the bisecting lines of the quarters of the circle, since the NURBS basis is not symmetric.

NURBS: $p = 2$.

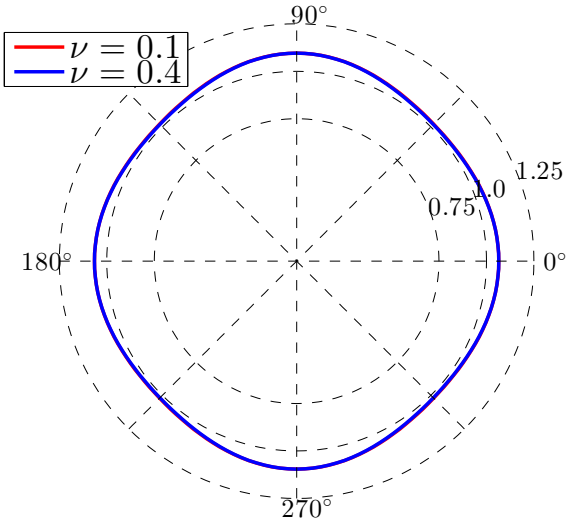

(a) $\widehat{e}_p(\boldsymbol{k})$ vs. ϑ for $\alpha = 0$

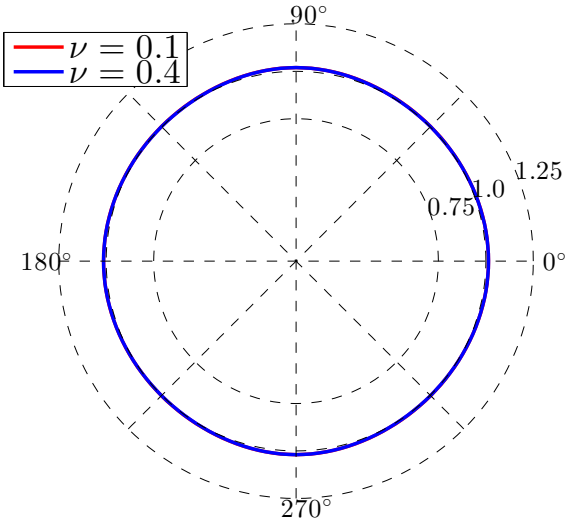

(b) $\widehat{e}_p(\boldsymbol{k})$ vs. ϑ for $\alpha = 1$

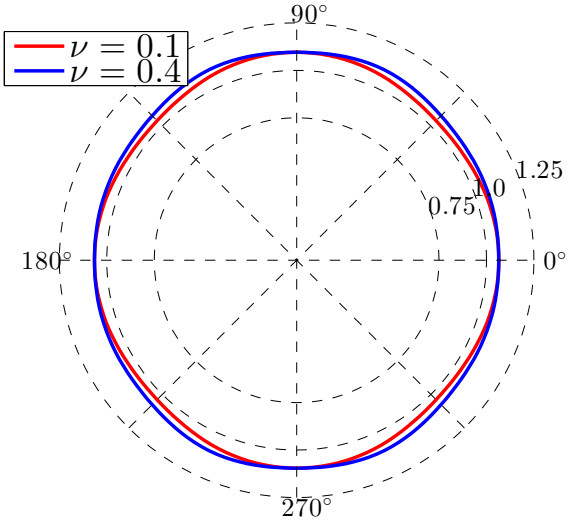

(c) $\widehat{e}_s(\boldsymbol{k})$ vs. ϑ for $\alpha = 0$

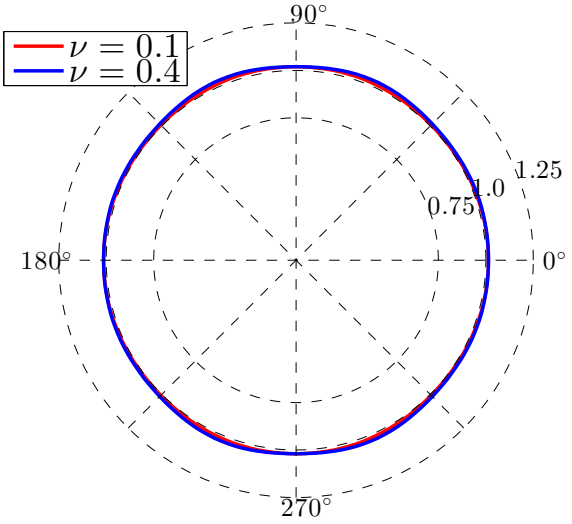

(d) $\widehat{e}_s(\boldsymbol{k})$ vs. ϑ for $\alpha = 1$

Figure 13: P– and S–waves velocity relative errors $\widehat{e}_p(\boldsymbol{k})$ (top) and $\widehat{e}_s(\boldsymbol{k})$ (bottom) vs. $\vartheta \in [0, 360°)$ ($\theta \in [0, 2\pi)$) in polar coordinates, obtained with $G = 4$ ($H = 0.25$), for $\nu = 0.1$ (blue) and $\nu = 0.4$ (red); NURBS basis functions of degree $p = 2$ and globally C^α–continuous with $\alpha = 0$ (left) and $\alpha = p - 1 = 1$ (right).

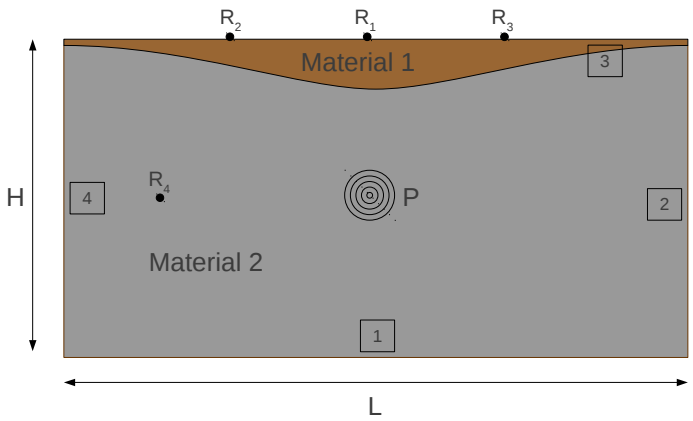

Figure 14: Sinusoidal type shaped valley for the simulation of the earthquake.

Material	$c_p \left[\frac{m}{s}\right]$	$c_s \left[\frac{m}{s}\right]$	$\rho \left[\frac{kg}{m^3}\right]$	$\zeta \left[\frac{1}{s}\right]$
1 ("soft")	$0.7000 \cdot 10^3$	$0.3500 \cdot 10^3$	$1.900 \cdot 10^3$	$3.141 \cdot 10^{-2}$
2 ("hard")	$3.500 \cdot 10^3$	$1.800 \cdot 10^3$	$2.200 \cdot 10^3$	$6.283 \cdot 10^{-2}$

Table 1: Material parameters for the simulation of the earthquake.

6 Simulation of Seismic Waves

We consider the numerical approximation of the elastodynamics equations presented in Sec. 2 by means of NURBS–based IGA in the framework of the Galerkin method with the aim of simulating the propagation of seismic waves in a portion of the earth mantle. In particular, we consider an earthquake event occurring in a sinusoidal valley, inspired by the problem proposed in [5, 15]; the two–dimensional computational domain under consideration is depicted in Fig. 14. Specifically, the simulation aims at reproducing a seismic event occurring in a valley composed of sediments as sandstone, namely "soft" material, deposited over the course of thousands of years on a bedrock of granite, namely "hard" material.

As anticipated, the computational domain $\Omega = (0, L) \times (0, H)$ is represented in Fig. 14, where $L = 2 \cdot 10^4\, m$ and $H = 10^4\, m$; the sinusoidal type valley of "soft" material is delimited by the B–spline curve $\mathbf{x}(\boldsymbol{\xi})$ (3.5) determined by the knot vector $\Xi = \{0, 0, 0, 1/5, 2/5, 3/5, 4/5, 1, 1, 1\}$ and control points $\boldsymbol{P}_1 = (0, H_{v1})^{\mathrm{T}}$, $\boldsymbol{P}_2 = (\Delta L_v, H_{v1})^{\mathrm{T}}$, $\boldsymbol{P}_3 = (2\Delta L_v, H_{v2})^{\mathrm{T}}$, $\boldsymbol{P}_4 = (3\Delta L_v, H_{v2})^{\mathrm{T}}$, $\boldsymbol{P}_5 = (4\Delta L_v, H_{v1})^{\mathrm{T}}$, and $\boldsymbol{P}_6 = (L, H_{v1})^{\mathrm{T}}$, where $H_{v1} = (H - 10^2)\, m$, $H_{v2} = (H - 10^3)\, m$, and $\Delta L_v = 4 \cdot 10^3\, m$. Homogeneous Neumann boundary conditions are considered for the top boundary of Ω, i.e. edge 3 in Fig. 14; on the edges 1, 2, and 4 the non–reflecting boundary conditions (2.4) are imposed with the aim of simulating the propagation of the seismic waves only in a limited part of the earth mantle, by avoiding significant reflections. The material properties are discontinuous across the interface representing the valley, as reported in Table 1; we remark that the "harder" material possesses higher compressional (c_p) and shear (c_s) wave velocities than the "softer" material. A point source of seismic excitation is placed in the rock region. Specifically, following [5], the forcing

term $\boldsymbol{f}$ of Eq. (2.1) is a point source load of the form:

$$\boldsymbol{f}(\mathbf{x},t) = \boldsymbol{d}(\mathbf{x})\, q(t), \tag{6.1}$$

where the function $\boldsymbol{d}$ describes a Dirac distribution function in space:

$$\boldsymbol{d}(\mathbf{x}) = \delta(\mathbf{x} - \boldsymbol{P})\, \widehat{\boldsymbol{d}}, \tag{6.2}$$

$\boldsymbol{P} = (10^4, 5 \cdot 10^3)^{\mathrm{T}}\, m$ is the source location, and $\widehat{\boldsymbol{d}} = (1,0)^{\mathrm{T}}$ the direction of the applied force; the function $q(t)$ in Eq. (6.1) represents the time history through a Ricker–type function defined as:

$$q(t) = q_0 \left(1 - 2\lambda(t-t_0)^2\right) \mathrm{e}^{-\lambda(t-t_0)^2}, \tag{6.3}$$

where $q_0 = 10^{10}\, Nm^{-2}$ is a suitable scaling factor, $t_0 = 2\, s$ is the time shift, and $\lambda = 9.8696\, s^{-1}$ is a parameter determining the "width" of the wavelet. We are interested in the seismic propagation of a time lapse of $30\, s$, for which $T = 30\, s$, starting from the initial conditions $\boldsymbol{u}_0 = \dot{\boldsymbol{u}}_0 = \mathbf{0}$.

For the spatial approximation we use NURBS–based Isogeometric Analysis in the framework of the Galerkin method. NURBS basis functions of polynomial degree $p = 2$ are used in both the parametric directions for representing the computational domain as well as for defining the finite dimensional NURBS function space $\mathcal{N}_h$ for the solution of problem (4.6). The NURBS basis functions are chosen as C^1–continuous in the computational domain Ω except across the curve representing the sinusoidal valley, where they are only C^0–continuous; such basis functions can be obtained as tensor product rule of the univariate B–splines basis depicted in Figs. 1(a) and (b) (see Sec. 3). We remark that the flexibility of NURBS basis functions in allowing the local reduction of the smoothness is particularly suitable in this case; indeed, the basis functions are only C^0–continuous through such interface, where the material properties are discontinuous and a reduced regularity of the solution is expected. The NURBS space $\mathcal{N}_h$ is composed of $N_{bf} = 13,780$ basis functions, with a quasi–uniform computational mesh with mesh elements of sizes indicatively $h_1 \simeq 20\, m$ in the basin and $h_2 \simeq 150\, m$ in the bedrock. For the time discretization we use the fully implicit, generalized–α method described in Sec. 4.2 for which we set the time step $\Delta t = 0.005\, s$ and $\rho_\infty = 0.5$ for the definition of the parameters α_m, α_f, β, and γ characterizing the method. Since the problem (2.1) is linear in the unknown $\boldsymbol{u}$, in the case of smooth solutions, we expect a second order convergence of the error with respect to the time discretization, as well as for the spatial approximation error in seminorm H^1, being basis functions of polynomial degree $p = 2$ used.

The propagation of the seismic waves in the earth mantle is illustrated in Fig. 15 at different times. We notice the propagation of the waves from the source point $\boldsymbol{P}$, where the forcing term is located, and an amplification of the wave, when the seismic waves enters into the "soft" material from the bedrock (Figs. 15(d) and (f)). In the Figs. 15(e)–(h) we observe that the main wave is reflected from the internal interface, where the material properties are discontinuous, and travels a second time upwards to the surface, without loosing a significant amount of energy. In Figs. 16 (a)–(h) we compare the horizontal and vertical displacements recorded at the receivers stations R_1–R_4 reported in Fig. 14; we remark that the receiver R_4 is placed at the same distance from the source location as the two receivers R_2 and R_3 and that the receivers R_1, R_2, and R_3 are located at the surface of the valley, i.e. the "soft" material region. By comparing the displacements recorded in R_1, R_2, and R_3 we confirm that the displacement of the material remains significant in magnitude for a longer period of time than in the bedrock material, where the amplitude of the seismic waves is damped in a shorter period of time. Indeed, we remark that most of the seismic waves do not cross the material interface immediately, but once entered in the "soft" material valley they are basically trapped inside at significant amplitude for longer time than in the bedrock.

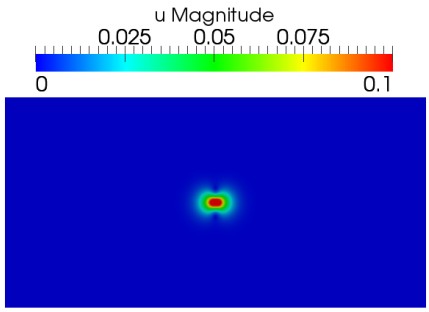

(a) $t = 1.5\,s$

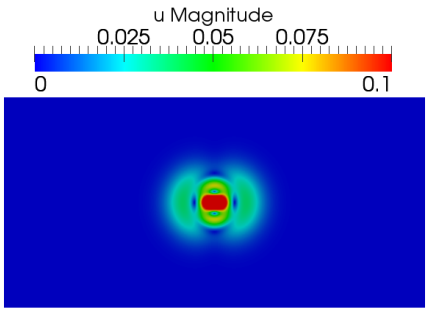

(b) $t = 2.0\,s$

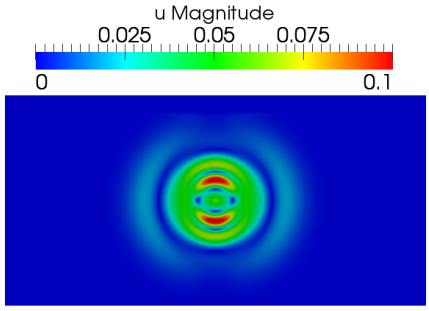

(c) $t = 2.5\,s$

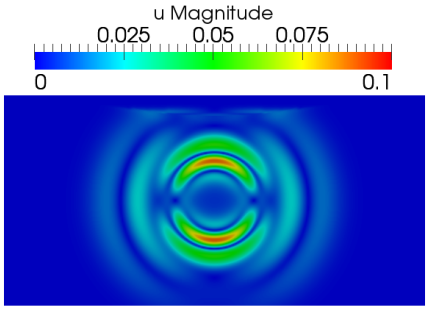

(d) $t = 3.0\,s$

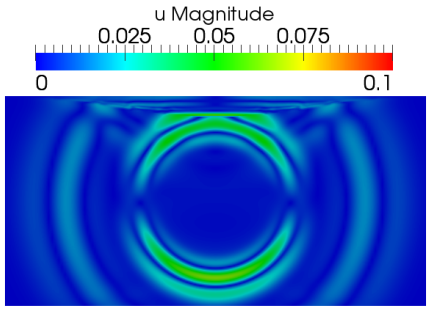

(e) $t = 4.0\,s$

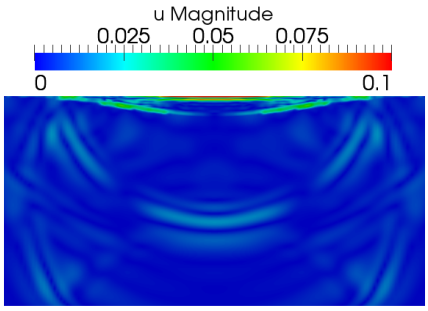

(f) $t = 7.0\,s$

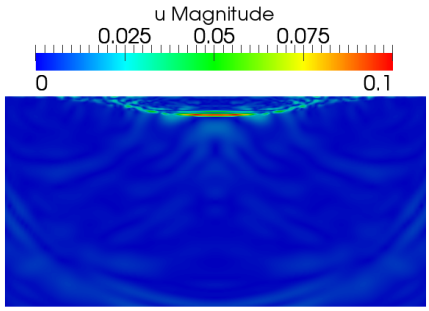

(g) $t = 10.0\,s$

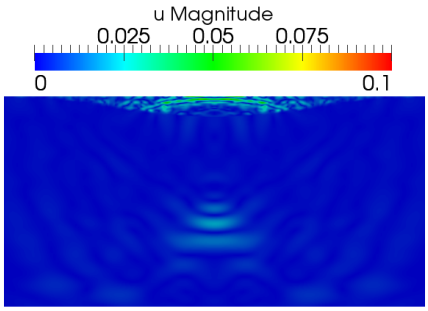

(h) $t = 13.0\,s$

Figure 15: Evolution of the seismic waves in the sinusoidal shaped valley: displacement magnitude $|\boldsymbol{u}|$ ($[m]$) at different times.

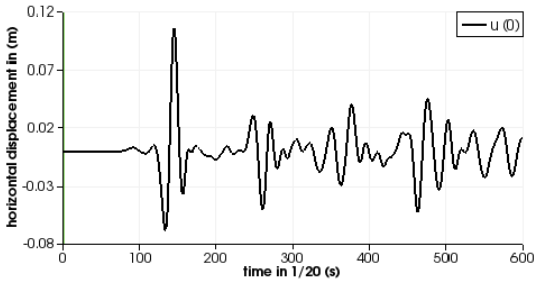

(a) Horizontal displacement recorded in R_1

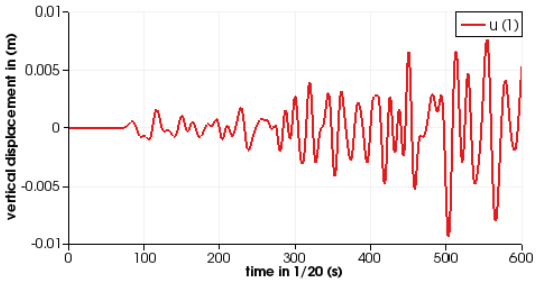

(b) Vertical displacement recorded in R_1

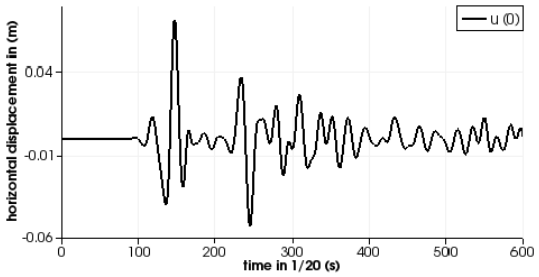

(c) Horizontal displacement recorded in R_2

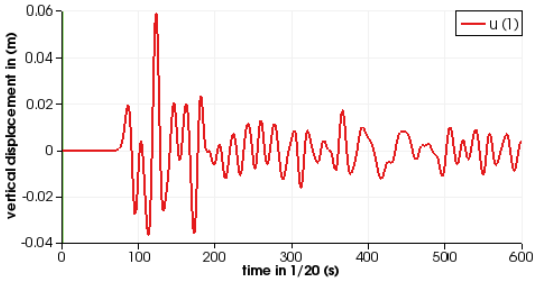

(d) Vertical displacement recorded in R_2

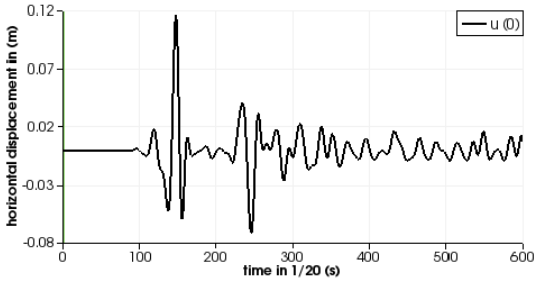

(e) Horizontal displacement recorded in R_3

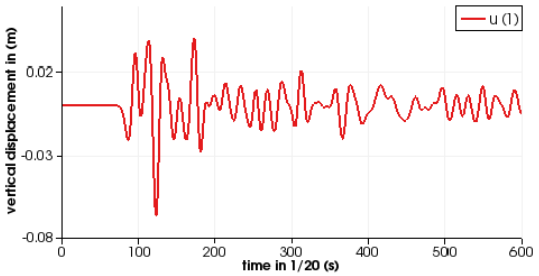

(f) Vertical displacement recorded in R_3

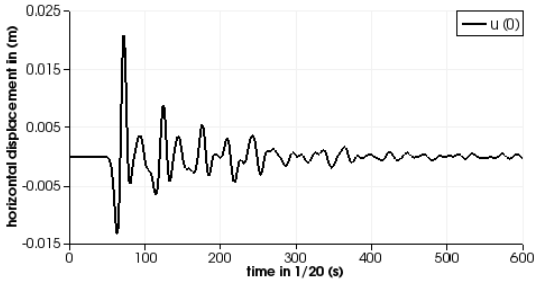

(g) Horizontal displacement recorded in R_4

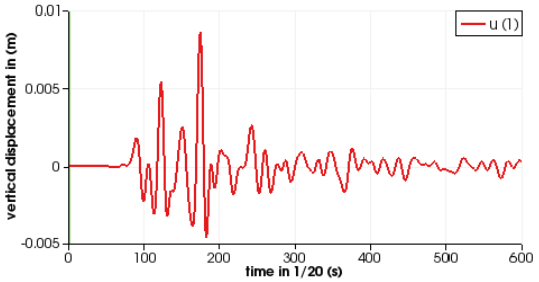

(h) Vertical displacement recorded in R_4

Figure 16: Computed horizontal u_1 and vertical u_2 displacements ($[m]$) vs. time t (scaled as $1/20\,s$) at the four receivers stations R_1, R_2, R_3, and R_4 highlighted in Fig. 14 (the displacements magnitudes are on different scales).

7 Conclusions

In this paper we numerically approximated the linear elastodynamics equations by means of NURBS–based Isogeometric Analysis (IGA) in the framework of the Galerkin method, for which we considered the numerical solution of elastic wave propagation problems, specifically in seismic applications. In particular, we carried out a numerical dispersion analysis for the elastodynamics equations, our focus being on the comparison of the use of globally C^0– and C^{p-1}–continuous NURBS basis functions, where p is the polynomial degree. In our discussion, we included the anisotropic curves for two–dimensional problems, i.e. the study of the errors associated to the compressional and shear wave velocities errors for different directions of the wave vector. Based on such dispersion analysis, we conclude that the use of globally C^{p-1}–continuous NURBS basis functions is more efficient than their C^0–continuous counterpart of polynomial degree p. In fact, the associated errors are significantly smaller when considering the same number of degrees of freedom. However, we remark that a complete analysis should involve the comparison of the computational costs associated to the use of NURBS basis functions with different regularity, a matter that should be further investigated.

Acknowledgements

We acknowledge Prof. P. Gervasio (Università degli Studi di Brescia), Dr. I. Mazzieri (MOX, Politecnico di Milano), and Dr. L. Gaudio (Universität Basel) for fruitful discussions and suggestions. The use of the Isogeometric GeoPDEs Library [25] for obtaining some of the numerical results reported in the paper is also acknowledged.

References

[1] R.A. Adams. *Sobolev Spaces*. Academic Press, New York, 1975.

[2] I. Akkerman, Y. Bazilevs, V.M. Calo, T.J.R. Hughes, and S. Hulshoff. The role of continuity in residual–based variational multiscale modeling of turbulence. *Computational Mechanics* **41**:371–378, 2008.

[3] M. Ainsworth. Discrete dispersion relation for *hp*–version finite element approximation at high wave number. *SIAM Journal on Numerical Analysis* **42**:553–575, 2004.

[4] M. Ainsworth, P. Monk, and W. Muniz. Dispersive and dissipative properties of discontinuous Galerkin finite element methods for the second–order wave equation. *Journal of Scientific Computing*, **27**:5–40, 2006.

[5] P.F. Antonietti, I. Mazzieri, A. Quarteroni, and F. Rapetti. Non–conforming high order approximations for the elastic wave equation. *Computer Methods in Applied Mechanics and Engineering* **209**:212–238, 2012.

[6] F. Auricchio, L. Beirão da Veiga, T.J.R. Hughes, A. Reali, and G. Sangalli. Isogeometric collocation methods. *Mathematical Models and Methods in Applied Sciences* **20**:2075–2107, 2010.

[7] F. Auricchio, F. Calabrò, T.J.R. Hughes, A. Reali, and G. Sangalli. A simple algorithm for obtaining nearly optimal quadrature rules for NURBS–based Isogeometric Analysis. *Computer Methods in Applied Mechanics and Engineering* **249–252**:15–27, 2012.

[8] Y. Bazilevs, L. Beirão da Veiga, J.A. Cottrell, T.J.R. Hughes, and G. Sangalli. Isogeometric Analysis: approximation, stability, and error estimates for h–refined meshes. *Mathematical Models and Methods for Applied Sciences* **16**:1031–1090, 2006.

[9] Y. Bazilevs, V.M. Calo, J.A. Cottrell, J.A. Evans, T.J.R. Hughes, S. Lipton, M.A. Scott, and T.W. Sederberg. Isogeometric analysis using T–splines. *Computer Methods in Applied Mechanics and Engineering* **199**:229–263, 2010.

[10] Y. Bazilevs, V.M. Calo, T.J.R. Hughes, and Y. Zhang. Isogeometric fluid-structure interaction: theory, algorithms, and computations. *Computational Mechanics* **43**:3–37, 2008.

[11] Y. Bazilevs, V.M. Calo, Y. Zhang, and T.J.R. Hughes. Isogeometric fluid–structure interaction analysis with applications to arterial blood flow. *Computational Mechanics* **38**:310–322, 2006.

[12] D.J. Benson, Y. Bazilevs, M.C. Hsu, and T.J.R. Hughes. *Isogeometric shell analysis: the Reissner-Mindlin shell. Computer Methods in Applied Mechanics and Engineering* **199**:276–289, 2010.

[13] C. Canuto, M.Y. Hussaini, A. Quarteroni, and T.A. Zang. *Spectral Methods. Evolution to Complex Geometries and Applications to Fluid Dynamics.* Springer, Berlin, 2007.

[14] C. Canuto, M.Y. Hussaini, A. Quarteroni, and T.A. Zang. *Spectral Methods. Fundamentals in Single Domains.* Springer–Verlag, Berlin, 2006.

[15] F. Casadei, E. Gabellini, G. Fotia, F. Maggio, and A. Quarteroni. A mortar spectral/finite element method for complex 2D and 3D elastodynamics problems. *Computer Methods in Applied Mechanics and Engineering* **191**:5119–5148, 2002.

[16] E.T. Chung and B. Engquist. Optimal discontinuous Galerkin methods for wave propagation. *SIAM Journal on Numerical Analysis* **44**:2131–2158, 2006.

[17] J. Chung and G.M. Hulbert. A time integration algorithm for structural dynamics with improved numerical dissipation: the generalized-α method. *Journal of Applied Mechanics*, **60**:371–375, 1993.

[18] J.A. Cottrell, T.J.R. Hughes, and Y. Bazilevs. *Isogeometric Analysis: Toward Integration of CAD and FEA*. Wiley, 2009.

[19] J.A. Cottrell, T.J.R. Hughes, and A. Reali. Studies of refinement and continuity in Isogeometric structural analysis. *Computer Methods in Applied Mechanics and Engineering* **196**:4160–4183, 2007.

[20] J.A. Cottrell, T.J.R. Hughes, A. Reali, and G. Sangalli. Isogeometric discretizations in structural dynamics and wave propagation. In *ECCOMAS Thematic Conference on Computational Methods in Structural Dynamics and Earthquake Engineering*, M. Papadrakakis, D.C. Charmpis, N.D. Lagaros, and Y. Tsompanakis (eds.), Rethymno, Crete, Greece, 13–16 June 2007.

[21] J.A. Cottrell, A. Reali, Y. Bazilevs, and T.J.R. Hughes. Isogeometric Analysis of structural vibrations. *Computer Methods in Applied Mechanics and Engineering* **195**:5257–5296, 2006.

[22] J.D. De Basabe and M.K. Sen. Comment on "Dispersion analysis of spectral element methods for elastic wave propagation" by G. Seriani and S.P. Oliveira. *Wave Motion* **46**:92–93, 2009.

[23] J.D. De Basabe, M.K. Sen, and M.F. Wheeler. The interior penalty discontinuous Galerkin method for elastic wave propagation: grid dispersion. *Geophysical Journal International* **175**:83–93, 2008.

[24] M. de Berg, O. Cheong, M. van Kreveld, and M. Overmars. *Computational Geometry: Algorithms and Applications*. Springer–Verlag, Heidelberg, 2008.

[25] C. de Falco, A. Reali, and R. Vázquez. GeoPDEs: a research tool for Isogeometric Analysis of PDEs. *Advances in Engineering Software* **42**:1020–1034, 2011.

[26] J.A. Evans, Y. Bazilevs, I. Babuška, and T.J.R. Hughes. n–widths, sup–infs, and optimality ratios for the k–version of the Isogeometric finite element method. *Computer Methods in Applied Mechanics and Engineering* **198**:1726–1741, 2009.

[27] H. Gómez, V.M. Calo, Y. Bazilevs, and T.J.R. Hughes. Isogeometric analysis of the CahnHilliard phase-field model. *Computer Methods in Applied Mechanics and Engineering* **197**:4333–4352, 2008.

[28] M.J. Grote, A. Schneebeli, and D. Schotzau. Discontinuous Galerkin finite element method for the wave equation. *SIAM Journal on Numerical Analysis* **44**:2408–2431, 2006.

[29] T.J.R. Hughes, J.A. Cottrell, and Y. Bazilevs. Isogeometric analysis: CAD, finite elements, NURBS, exact geometry and mesh refinement. *Computer Methods in Applied Mechanics and Engineering* **194**:4135–4195, 2005.

[30] T.J.R. Hughes, A. Reali, and G. Sangalli. Duality and unified analysis of discrete approximations in structural dynamics and wave propagation: Comparison of p–method finite elements with k–method NURBS. *Computer Methods in Applied Mechanics and Engineering* **197**:4104–4124, 2008.

[31] T.J.R. Hughes, A. Reali, and G. Sangalli. Efficient quadrature for NURBS–based Isogeometric Analysis. *Computer Methods in Applied Mechanics and Engineering* **199**:301–313, 2010.

[32] S. Lipton, J.A. Evans, Y. Bazilevs, T. Elguedj, and T.J.R. Hughes. Robustness of Isogeometric structural discretizations under severe mesh distortion. *Computer Methods in Applied Mechanics and Engineering* **199**:357–373, 2010.

[33] J. Liu, L. Dedè, J.A. Evans, M.J. Borden, and T.J.R. Hughes. Isogeometric Analysis of the advective Cahn–Hilliard equation: spinodal decomposition under shear flow. *Journal of Computational Physics* **242**:321–350, 2013.

[34] I. Mazzieri and F. Rapetti. Dispersion analysis of triangle–based spectral element methods for elastic wave propagation. *Numerical Algorithms* **60**:631–650, 2012.

[35] L. Piegl and W. Tiller. *The NURBS Book*. Springer–Verlag, New York, 1997.

[36] A. Quarteroni, R. Sacco, and F. Saleri. *Numerical Mathematics*. Springer, Berlin and Heidelberg, 2007.

[37] A. Quarteroni and A. Valli. *Numerical Approximation of Partial Differential Equations*. Springer–Verlag, Berlin and Heidelberg, 1994.

[38] A. Reali. An Isogeometric Analysis approach for the study of structural vibrations. *Journal of Earthquake Engineering* **10**:1–30, 2006.

[39] B. Rivière, S. Shaw, M.F. Wheeler, and J.R. Whiteman. Discontinuous Galerkin finite element methods for linear elasticity and quasistatic linear viscoelasticity. *Numerische Mathematik* **95**:347–376, 2003.

[40] D. Schillinger, J.A. Evans, A. Reali, M.A. Scott, and T.J.R. Hughes. Isogeometric collocation: cost comparison with Galerkin methods and extension to adaptive hierarchical NURBS discretizations. *Computer Methods in Applied Mechanics and Engineering* **267**:170–232, 2013.

[41] T.W. Sederberg, J. Zheng, A. Bakenov, and A. Nasri. T–splines and T–NURCCs. *ACM Transactions on Graphics*, **22**:477-484, 2003.

[42] G. Seriani, S.P. Oliveira. Dispersion analysis of spectral element methods for elastic wave propagation. *Wave Motion* **45**:729–744, 2008.

[43] R. Stacey. Improved transparent boundary formulations for the elastic–wave equation. *Bulletin of the Seismological Society of America* **78**:2089–2097, 1988.

[44] A. Tagliabue, L. Dedè, and A. Quarteroni. Isogeometric analysis and error estimates for high order Partial Differential Equations in fluid dynamics. *MATHICSE report* **37.2012**, 2012 and *MOX report* **27.2013**, 2013.

[45] L.L. Thompson. A review of Finite Element methods for time–harmonic acoustics. *Journal of the Acoustical Society of America* **119**:1315–1330, 2006.

[46] Y. Zhang, Y. Bazilevs, S. Goswami, C.L. Bajaj, and T.J.R. Hughes. Patient–specific vascular NURBS modeling for Iisogeometric analysis of blood flow. *Computer Methods in Applied Mechanics and Engineering* **196**:2943–2959, 2007.

Recent publications:

MATHEMATICS INSTITUTE OF COMPUTATIONAL SCIENCE AND ENGINEERING
Section of Mathematics
Ecole Polytechnique Fédérale
CH-1015 Lausanne

07.2014 ASSYR ABDULLE, YUN BAI:
Reduced order modelling numerical homogenization

08.2014 ANDREA MANZONI, FEDERICO NEGRI:
Rigorous and heuristic strategies for the apporximation of stability factors in nonlinear parametrized PDEs

09.2014 PENG CHEN, ALFIO QUARTERONI:
A new algorithm for high-dimensional uncertainty quantification problems based on dimension-adaptive and reduced basis methods

10.2014 NATHAN COLLIER, ABDUL-LATEEF HAJI-ALI, FABIO NOBILE, ERIK VON SCHWERIN, RAÚL TEMPONE:
A continuation multilevel Monte Carlo algorithm

11.2014 LUKA GRUBISIC, DANIEL KRESSNER:
On the eigenvalue decay of solutions to operator Lyapunov equations

12.2014 FABIO NOBILE, LORENZO TAMELLINI, RAÚL TEMPONE:
Convergence of quasi-optimal sparse grid approximation of Hilbert-valued functions: application to random elliptic PDEs

13.2014 REINHOLD SCHNEIDER, ANDRÉ USCHMAJEW:
Convergence results for projected line-search methods on varieties of low-rank matrices via Lojasiewicz inequality

14.2014 DANIEL KRESSNER, PETAR SIRKOVIC:
Greedy law-rank methods for solving general linear matrix equations

15.2014 WISSAM HASSAN, MARCO PICASSO:
An anisotropic adaptive finite element algorithm for transonic viscous flows around a wing

16.2014 ABDUL-LATEEF HAJI-ALI, FABIO NOBILE, ERIK VON SCHWERIN, RAÚL TEMPONE:
Optimization of mesh hierarchies in multilevel Monte Carlo samplers

17.2014 DANIEL KRESSNER, FRANCISCO MACEDO:
Low-rank tensor methods for communicating Markov processes

18.2014 ASSYR ABDULLE, GILLES VILMART, KONSTANTINOS C. ZYGALAKIS:
Long time accuracy of Lie-Trotter splitting methods for Langevin dynamics

19.2014 ELEONORA MUSHARBASH, FABIO NOBILE, TAO ZHOU:
Con the dynamically orthogonal approximation of time dependent random PDEs

20.2014 FROILÁN M. DOPICO, JAVIER GONZÁLEZ, DANIEL KRESSNER, VALERIA SIMONCINI:
Projection methods for large T-Sylvester equations

21.2014 LUCA DEDÈ, CHRISTOPH JÄGGLI, ALFIO QUARTERONI:
Isogeometric numerical dispersion analysis for elastic wave propagation